LONG WAVELENGTH INFRARED MERCURY CADMIUM TELLURIDE PHOTODIODES AND FOCAL PLANE ARRAYS

A THESIS SUBMITTED TO
THE GRADUATE SCHOOL OF NATURAL AND APPLIED SCIENCES
OF
MIDDLE EAST TECHNICAL UNIVERSITY

BY

BURAK AŞICI

IN PARTIAL FULFILLMENT OF THE REQUIREMENTS
FOR
THE DEGREE OF MASTER OF SCIENCE
IN
ELECTRICAL AND ELECTRONICS ENGINEERING

SEPTEMBER 2005

Approval of Graduate School of Natural and Applied Sciences.

_____

Prof. Dr. Canan ÖZGEN

Director

I certify that this thesis satisfies all the requirements as a thesis for the degree of Master of Science.

_____

Prof. Dr. İsmet ERKMEN

Head of Department

We certify that we have read this thesis and that in our opinion it is fully adequate, in scope and quality, as a thesis for the degree of Master of Science.

_____

Prof. Dr. Cengiz BEŞİKCİ

Supervisor

Examining Committee Members:

Prof. Dr. Tayfun AKIN	(METU, EE)	_____
Prof. Dr. Cengiz BEŞİKCİ	(METU, EE)	_____
Prof. Dr. Nevzat G. GENÇER	(METU, EE)	_____
Asst. Prof. Dr. Haluk KÜLAH	(METU, EE)	_____
Prof. Dr. Mehmet PARLAK	(METU, Physics)	_____

I hereby declare that all information in this document has been obtained and presented in accordance with academic rules and ethical conduct. I also declare that, as required by these rules and conduct, I have fully cited and referenced all material and results that are not original to this work.

Name, Last name:

Signature :

ABSTRACT

LONG WAVELENGTH INFRARED MERCURY CADMIUM TELLURIDE PHOTODIODES AND FOCAL PLANE ARRAYS

AŞICI, Burak

M.Sc., Department of Electrical and Electronics Engineering

Supervisor: Prof. Dr. Cengiz BEŞİKCİ

September 2005, 75 pages

This thesis reports the fabrication and characterization of long wavelength infrared mercury cadmium telluride ($Hg_{1-x}Cd_xTe$) photodiodes and 128x128 focal plane arrays grown on lattice matched cadmium zinc telluride ($Cd_{1-y}Zn_yTe$) substrates by metal organic vapor phase epitaxy (MOVPE). The dark current modeling of 33x33 μm^2 $Hg_{1-x}Cd_xTe$ photodiodes has shown the dark current is dominated by trap assisted tunneling under small reverse bias voltages typically used to bias these detectors. The dominant dark current mechanisms under high reverse bias and low forward bias are band–to–band tunneling and generation–recombination, respectively. The photodiodes have yielded a peak 77 K detectivity of $3.2x10^{10}$ cm$\sqrt{Hz}$/W with a cut-off wavelength (50%) of 10.92 μm. It has also been found that the 1/f noise current of the detectors at 1 Hz is related to

the trap-assisted tunneling current through the empirical relation $i_n=\alpha_{TAT}(I_{TAT})^{\beta}$ with $\alpha_{TAT}=7.0\ x\ 10^{-5}$ and $\beta=0.65$.

In the course of the focal plane array (FPA) fabrication process development work, ohmic contact formation on p-type $Hg_{1-x}Cd_xTe$ and mesa wet etch were studied in detail. Contacts with chromium, gold, platinum and copper on p-type $Hg_{1-x}Cd_xTe$ resulted in bad ohmic contacts, which did not seem to improve with annealing. On the other hand a HgTe cap layer on p-type $Hg_{1-x}Cd_xTe$ resulted in good ohmic contact with acceptably low resistance. Among the etchants studied for mesa etching of the diode structures, Br_2/HBr solution yielded the best performance.

After developing all of the steps of FPA processing, 128x128 $Hg_{1-x}Cd_xTe$ FPAs were successfully fabricated and tested in a thermal imager. While thermal imaging was performed with the FPAs, high nonuniformity of the material and low R_0A product of the pixels did not allow high sensitivity imaging.

Keywords: Mercury Cadmium Telluride, focal plane array, cooled infrared detector

ÖZ

UZUN DALGABOYU KIZILÖTESİ CIVA KADMİYUM TELLÜR FOTODİYOT VE ODAK DÜZLEM MATRİSLERİ

AŞICI, Burak
Yüksek Lisans, Elektrik ve Elektronik Mühendisliği Bölümü
Tez Yöneticisi: Prof. Dr. Cengiz BEŞİKCİ

Eylül 2005, 75 sayfa

Bu tezde metal organik gaz fazı epitaksisi (MOGFE) ile örgü uyumlu kadmiyum çinko tellür tabanlar üzerine büyütülmüş olan uzun dalga boyu kızılötesi cıva kadmiyum tellür ($Hg_{1-x}Cd_xTe$) fotodiyot ve 128x128 odak düzlem matrislerinin fabrikasyonu ve karakterizasyonu rapor edilmektedir. 33x33 μm^2 $Hg_{1-x}Cd_xTe$ fotodiyotların karanlık akım modellemesi, bu diyotların eğimlemesi için tipik olarak kullanılan düşük ters eğimleme gerilimleri altında tuzak yardımlı tünelleme mekanizmasının en etkili karanlık akım mekanizması olduğunu göstermiştir. Yüksek ters eğimleme ve küçük ileri eğimleme altında baskın karanlık akım mekanizmaları sırasıyla banttan banda tünelleme ve çoğalma–birleşmedir. 10.92 μm kesim dalga boyuna (%50) sahip fotodiyotlar 77 K'de $3.2x10^{10}$ cm√Hz/W tepe dedektivite değeri vermiştir. Dedektörlerin 1 Hz'deki 1/f gürültü akımının

$i_n=\alpha_{TAT}(I_{TAT})^{\beta}$ ampirik denklemi ($\alpha_{TAT}=7.0\ 10^{-5}$ ve $\beta=0.65$ olmak üzere) ile tuzak yardımlı tünelleme akımına bağlı olduğu gözlenmiştir.

Odak düzlem matrisi (ODM) fabrikasyon proseslerinin geliştirilmesi esnasında, p-tipi $Hg_{1-x}Cd_xTe$ üzerinde omik kontak oluşturulması ve mesa ıslak aşındırılması üzerine detaylı olarak çalışılmıştır. Krom, altın, platin ve bakır ile p-tipi $Hg_{1-x}Cd_xTe$ üzerinde, tavlama uygulanmasına rağmen düzelmeyen, kötü omik kontaklar oluşmuştur. Diğer yandan, p-tipi $Hg_{1-x}Cd_xTe$'ün üzerinde büyütülen bir HgTe katmanı ile kabul edilebilecek seviyede düşük dirence sahip omik kontaklar oluşturulmuştur. Diyot yapılarının mesa aşındırmasında kullanılmak için üzerinde çalışılan aşındırıcılardan, Br_2/HBr çözeltisi en iyi performansı vermiştir.

ODM proses adımlarının geliştirilmesinin ardından, 128x128 $Hg_{1-x}Cd_xTe$ ODM'ler başarıyla fabrike edilmiş ve bir termal görüntüleyicide test edilmiştir. ODM'ler ile termal görüntüleme yapılmış olmasına rağmen, malzemenin yüksek düzensizliği ve piksellerin düşük R_0A çarpımı yüksek hassasiyette görüntüleme yapılmasına izin vermemiştir.

Anahtar Kelimeler: Cıva Kadmiyum Tellür, odak düzlem matrisi, soğutmalı kızılötesi dedektör

To my family and Tuğba

ACKNOWLEDGMENTS

I would like to thank my thesis supervisor Prof. Dr. Cengiz Beşikci for his guidance and support during my thesis study. I also would like to thank Selçuk Özer who shared his invaluable process experience with me. I am pleased to thank Oray Orkun Cellek for his help in the optical characterization and noise measurements of photodetectors. I must express my deepest gratitude to Ümid Tümkaya for sharing his invaluable experience in dark current modeling of photodiodes.

I would like to thank Professor Józef Piotrowski and VIGO System S.A. for their discussion about ohmic contacts to $Hg_{1-x}Cd_xTe$ and for providing HgTe deposition service to our $Hg_{1-x}Cd_xTe$ samples. I am more than grateful for their assistance.

For my family, I could never say enough to show my gratitude and appreciation for their invaluable support and motivation.

Finally, I would like to thank ASELSAN Inc. and the Research, Development and Technology Department of the Ministry of Defense for funding this research study.

TABLE OF CONTENTS

ABSTRACT ..... **iv**

ÖZ ..... **vi**

ACKNOWLEDGMENTS ..... **ix**

TABLE OF CONTENTS ..... **x**

CHAPTERS

1. INTRODUCTION **1**

1.1 Infrared Radiation 2

1.2 Infrared Detectors 5

1.2.1 Thermal Detectors 5

1.2.2 Photon Detectors 6

1.3 Figures of Merit for Infrared Detectors and Focal Plane Arrays 8

1.3.1 Responsivity 9

1.3.2 Noise Equivalent Power 9

1.3.3 Detectivity 9

1.3.4 Noise Equivalent Temperature Difference (NETD) 10

1.3.5 Time Constant 10

2. MERCURY CADMIUM TELLURIDE INFRARED DETECTORS AND FOCAL PLANE ARRAYS **11**

2.1 History of $Hg_{1-x}Cd_xTe$ 11

2.2 Material Related Issues 12

2.3 $Hg_{1-x}Cd_xTe$ Growth 15

2.4 $Hg_{1-x}Cd_xTe$ InfraredDetectors and Focal Plane Arrays 16

2.4.1 Planar $Hg_{1-x}Cd_xTe$ Detectors 16

2.4.2 Double Layer Heterojunction $Hg_{1-x}Cd_xTe$ Detectors 17

2.4.3 Loophole $Hg_{1-x}Cd_xTe$ Detectors 17

2.5 Comparison of Alternative Technologies 18

2.6 State of the Art $Hg_{1-x}Cd_xTe$ FPAs 19

3. MERCURY CADMIUM TELLURIDE EPILAYER STRUCTURES 20

3.1 Epilayer Structures and Design Considerations 21

3.1.1 Structure 1 22

3.1.2 Structure 2 26

3.2 Comparison of n^+-on-p and p^+-on-n Detector Structures 26

4. DEVELOPMENT OF FOCAL PLANE ARRAY FABRICATION PROCESS AND 128x128 MERCURY CADMIUM TELLURIDE FOCAL PLANE ARRAY FABRICATION 29

4.1 128x128 $Hg_{1-x}Cd_xTe$ FPA Fabrication Steps 31

4.1.1 Mesa Etch Study 32

4.1.2 Ohmic Contact Study 39

4.1.2.1Chromium (Cr) Contacts 40

4.1.2.2 Gold (Au) Contacts 41

4.1.2.3 Platinum (Pt) Contacts 42

4.1.2.4 Copper (Cu) Contacts 43

4.1.2.5 HgTe Contacts 43

4.2 128x128 $Hg_{1-x}Cd_xTe$ FPA Fabrication 44

4.2.1 Alignment Mark Process 44

4.2.2 Mesa Etch Process 45
4.2.3 Metal Contact Deposition Process 46
4.2.4 Pasivation Material Deposition and Etch Process 47
4.2.5 Under Bump Metal (UBM) Deposition Process 47
4.2.6 Indium (In) Electroplating Process 47
4.2.7 ROIC Post Processing 48
4.2.8 Flip-Chip Bonding of FPA and ROIC 49
5. FOCAL PLANE ARRAY AND PIXEL CHARACTERISTICS 50
5.1 Electrical and Optical Measurement Set Ups 50
5.2 $Hg_{1-x}Cd_xTe$ Photodiode Characteristics 52
5.2.1 Electrical Characteristics 53
5.2.2 Optical Characteristics 54
5.2.3 Dark Current Modeling 55
5.2.3.1 Diffusion Current 56
5.2.3.2 Generation-Recombination Current 56
5.2.3.3 Tunneling Current 58
5.2.3.4 Ohmic Leakage Current 59
5.2.3.5 Dark Current Analysis 59
5.2.4 Detector Noise Analysis 62
5.3 Real Time Thermal Imaging with 128 x 128 $Hg_{1-x}Cd_xTe$ FPAs 66
6. CONCLUSIONS 69
REFERENCES 71

CHAPTER 1

INTRODUCTION

The detectors sensing in the mid-wavelength infrared (MWIR, 3-5 μm) and long-wavelength infrared (LWIR, 8-14 μm) regions of the electromagnetic spectrum are important for both military and civil thermal imaging applications. Having an adjustable energy bandgap in a wide range in the infrared wavelengths, mercury cadmium telluride ($Hg_xCd_{1-x}Te$) has been a very important semiconductor for both MWIR and LWIR sensors. While the material is difficult to handle and process, it is still the most widely utilized semiconductor for thermal imaging, especially in the LWIR band. $Hg_{1-x}Cd_xTe$ has been studied in detail since late 1950s. However, there is still significant amount of work being reported on the characteristics of the material and the detectors fabricated with it, high quality growth of $Hg_{1-x}Cd_xTe$ on alternative substrates, and $Hg_{1-x}Cd_xTe$ focal plane arrays (FPAs). This thesis reports the development of fabrication process for long wavelength infrared (LWIR) homojunction and heterojuction $Hg_{1-x}Cd_xTe$ 128x128 (FPAs), as well as the characteristics of p on n $Hg_{1-x}Cd_xTe$ detectors having the same size (33x33 μm^2) and structure with the FPA pixels. This study incorporates the optimization of each step of the FPA fabrication process starting

with mesa etch and ending with flip-chip bonding of the detector array with the read-out integrated circuit (ROIC). The ROIC employed in this study is a commercial one (ISC9806) produced by Indigo Systems Inc.

This thesis is organized as follows. This chapter is devoted to a brief and general introduction of infrared sensors and imaging. More detailed discussion on the topics introduced in this chapter can be accessed through the listed references in this chapter. Chapter 2 summarizes the properties of $Hg_{1-x}Cd_xTe$, describes the types of $Hg_{1-x}Cd_xTe$ detectors and discusses the current status of the $Hg_{1-x}Cd_xTe$ FPA technology. Chapter 3 introduces and discusses the $Hg_{1-x}Cd_xTe$ epilayer structures employed in this work for the fabrication of the above mentioned focal plane arrays. The development of the 128x128 FPA fabrication procedure and process descriptions are given in Chapter 4. The pixel characteristics of the fabricated 128x128 FPA are presented and discussed in Chapter 5. Finally, Chapter 6 presents the conclusion and future work.

In the following section, basics of infrared radiation, infrared detectors, and fundamental figures of merit for the evaluation of infrared detectors are summarized before concentrating the discussion on $Hg_{1-x}Cd_xTe$ detectors in Chapter 2.

1.1 Infrared Radiation

The presence of the infrared radiation was discovered by Sir William Herschel in 1800. He used a prism to disperse sunlight into its spectral components and put a thermometer under different colored rays to study the energy distribution of the spectrum of sunlight. He observed temperature rise when he put the thermometer beyond the red end of the visible spectrum. From this experiment, he concluded that spectral components of light also include some form of invisible rays [1]. The part of the electromagnetic spectrum between the visible and the microwave regions is the infrared region extending from 0.7 μm to 1000 μm.

Every object with temperature greater than the absolute zero radiates electromagnetic radiation. Planck's law of blackbody radiation gives the temperature dependence of radiation of an object. In the case of an ideal blackbody, the spectral exitance, which is the power emitted per unit area per unit wavelength ($Jm^{-3}sec^{-1}$) is given by [2]

$$\frac{dR(\lambda,T)}{d\lambda} = \frac{2\pi hc^2\lambda^{-5}}{e^{hc/\lambda kT} - 1} \tag{1.1}$$

where T is the blackbody temperature (K), h is the Planck's constant (J sec), λ is the wavelength (m), k is the Boltzmann's constant (J/K), and c is the speed of light (m/sec). Wien's law of displacement gives the wavelength of peak emission from a blackbody with temperature T [2]

$$\lambda_{\max} = \frac{2898}{T} \tag{1.2}$$

where λ_{max} is the wavelength of peak emission (μm), and T is the blackbody temperature (K). In Figure 1.1, blackbody spectrum as a function of wavelength for various temperatures is given. It can be seen that maximum emission of infrared radiation occurs at about 10 μm wavelength for objects at room temperature (about 300 K). As the temperature of the object increases, the peak emission wavelength decreases towards the visible portion of the electromagnetic spectrum whereas the spectral energy density increases significantly.

The radiation emitted or reflected from the targets and backgrounds must pass through intervening atmosphere before reaching the detection system. Molecules such as H_2O, CO_2, O_2, CO, O_3, CH_4, N_2O absorb infrared radiation at some specific wavelengths. Thus the transmission of infrared radiation through atmosphere at these wavelengths is very poor. Atmospheric transmission spectrum at sea level as a function of wavelength is given in Figure 1.2 [3].

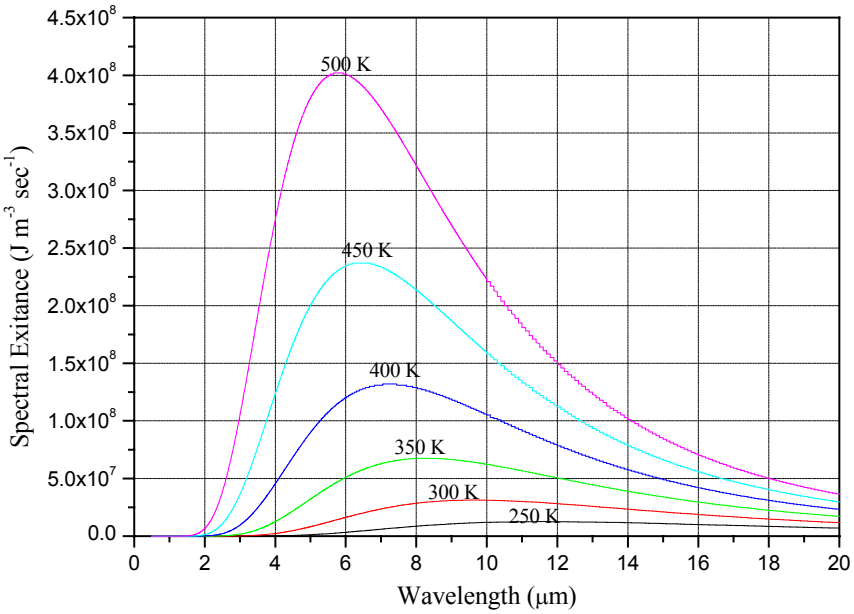

Figure 1.1: Spectral exitance of a blackbody as a function of wavelength for different blackbody temperatures.

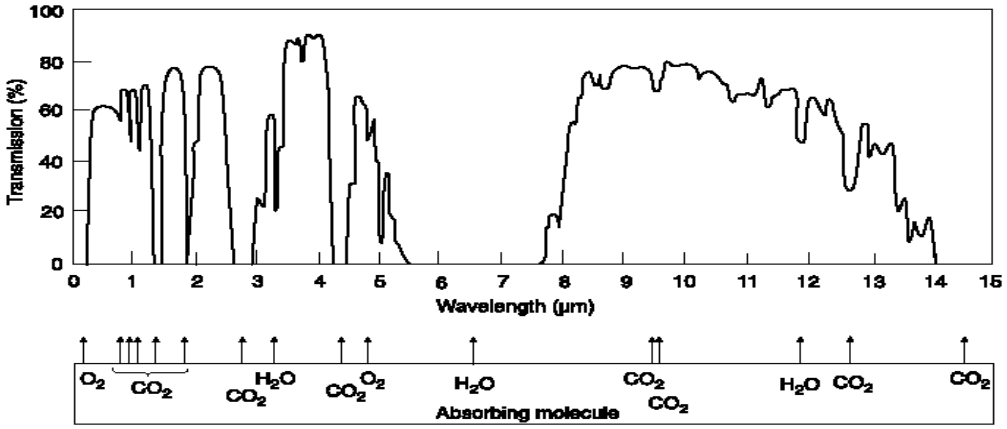

Figure 1.2: Transmittance of atmosphere over 6000 ft sea level path [3].

It can be seen from Figure 1.2 that there exists some wavelength bands in which atmospheric absorption is very small. These windows are given in Table 1.1. LWIR band (8.0 –14.0 μm) is important for thermal imaging since the Wien displacement law (Equation 1.2) states that maximum emission of infrared radiation for objects near room temperature occurs in this band. Also LWIR band

offers good transmission of infrared radiation through mist and smoke. On the other hand, MWIR band (3.0–5.5 μm) is more appropriate for hotter objects (i.e., temperatures in the range of 580 K–970 K). Even though the sensitivity of LWIR band is better for room temperature objects, the MWIR band yields greater contrast [3].

Table 1.1: Subregions of Infrared Radiation [4].

Bands (Abbreviation)	**Wavelength Range (μm)**
Near Infrared (NIR)	0.7 – 1.1
Short Wavelength Infrared (SWIR)	1 .1 – 2.5
Mid Wavelength Infrared (MWIR)	3.0 – 5.5
Long Wavelength Infrared (LWIR)	8.0 – 14.0

1.2 Infrared Detectors

An infrared detector is simply a transducer of radiant energy in the infrared into a measurable form. Generally infrared detectors are divided into two classes: thermal detectors and photon detectors.

1.2.1 Thermal Detectors

In thermal detectors absorption of infrared radiation heats the detector causing a change in detector's temperature. The temperature change causes variation in some properties of the material, and this variation can be sensed electronically. Therefore, the detector's output does not depend on the photon nature of the incident radiation [5]. The major advantage of thermal detectors is their ability to operate without cooling. However the sensitivity of thermal detectors is lower, and the response time is longer. There are different types of thermal detectors such as bolometers, pyroelectric detectors, thermoelectric devices, and Golay detectors.

A resistive bolometer consists of a resistive element whose resistance changes with varying temperature. Semiconductors such as vanadium oxide, amorphous

silicon, and polycrystalline silicon are used as resistive element in infrared bolometers due to their high temperature coefficient of resistivity [6].

A pyroelectric detector contains certain dielectric materials with low crystal symmetry. Thermal changes alter the electrical polarization, which causes a voltage difference. Common pyroelectric materials used for detectors are tri-glycine sulphate (TGS), lithium tantalate ($LiTaO_3$), lead zinc titanate (PZT) [6].

Thermoelectric devices such as thermocouples and thermopiles are based on the presence of one or several junctions between two metals. A thermopile is a group of thermocouples connected in series. Thermocouples make use of the Peltier-Seebeck effect, which is the induction of voltage due to thermal gradient across a conductor. In order to increase the sensitivity, materials that yield higher Seebeck coefficient should be preferred [6].

The Golay detector's detecting principle depends on volume or pressure variation of an encapsulated gas with temperature [6].

1.2.2 Photon Detectors

In photon detectors absorption of infrared radiation is due to the interaction of incident photons with electrons, either bound to lattice atoms, or impurity atoms or with free electrons. These processes are shown in Figure 1.3 [5]. Photon detectors exhibit high detectivity, as well as small response time, and the responsivity of photon detectors displays wavelength dependence. Photon detectors can be divided into different types with respect to the nature of the electron-photon interaction as intrinsic, extrinsic, free carriers, and quantum well detectors. It is also possible to classify photon detectors with respect to electrical output of the detector as photoconductive, photovoltaic, capacitance and photoelectromagnetic. The most important types of photon detectors with respect to electrical output classification are photoconductive and photovoltaic detectors.

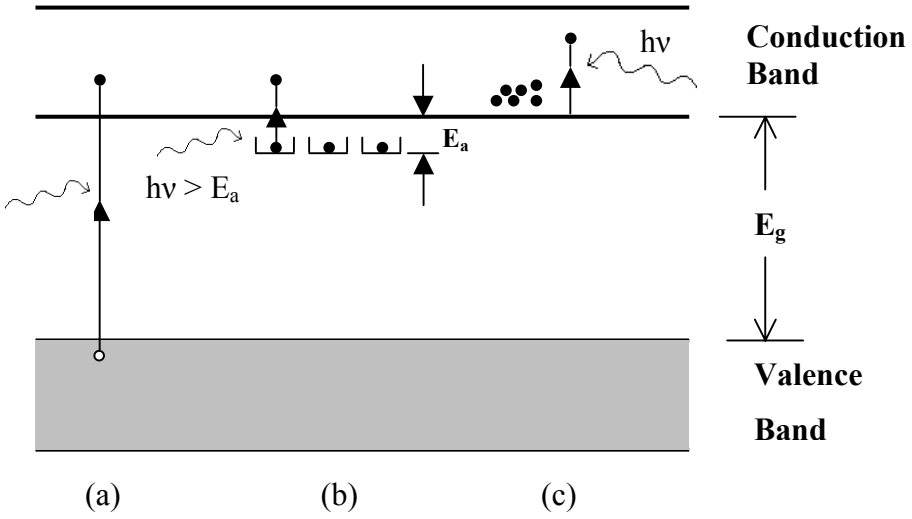

Figure 1.3: Fundamental optical excitation processes in the semiconductors: (a) intrinsic absorption, (b) extrinsic absorption, (c) free carrier absorption [5].

In intrinsic detectors the photo-transition takes place across the fundamental band gap of the detector material, which puts a limit on the detection wavelength. Response of the detector drops very rapidly for photons with energy lower than the energy band gap of the detector material. With respect to the electrical output of the detector, intrinsic type detectors can be photoconductive or photovoltaic.

Operating principle of photoconductive devices depends on photo-generation of charge carriers. The conductivity of the material increases due to photo-generated charge carriers. In order to avoid the recombination of the photo-generated charge carriers, sufficiently large bias must be applied to the detector. While, photoconductive type detectors may yield high responsivity, they are not proper for dense focal plane arrays due to large bias and current levels required.

A photovoltaic detector has an internal potential barrier with a built-in electric field. The role of the built-in electric field is to separate the charge carriers with opposite signs. Such potential barriers can be created by the use of p-n junctions, heterojunctions, Schottky barriers, and metal-insulator-semiconductor (MIS) photo-capacitors. The most important and common example of a photovoltaic detector is a photodiode, which is simply a p-n junction [5]. Photodiodes can be

operated under zero bias or in reverse bias. Slight reverse bias is usually preferred in order to achieve a large dynamic diode resistance. Photovoltaic type detectors are usually preferred over photoconductive ones for medium to very large format focal plane arrays.

In extrinsic detectors photo transition takes place from impurity states to either of the valence band or the conduction band. The energy level of the doped impurities such as silicon or germanium puts a limit on the detection wavelength. All of the extrinsic detectors operate as a photoconductors. The most important disadvantage of extrinsic type detectors is the necessity of cooling down to very low temperatures such as liquid helium temperature in order to achieve reasonably low noise levels.

The most commonly used semiconductors for MWIR detectors are $Hg_{1-x}Cd_xTe$ and InSb, while HgCdTe has almost been the only choice for LWIR sensors until recently. Today, $Hg_{1-x}Cd_xTe$ is competing with recently emerged Quantum Well Infrared Photodetector (QWIP) technology, which utilizes more mature semiconductor systems such as AlGaAs/GaAs. In a QWIP, the detection mechanism relies on the interaction of photons with bound electrons in a semiconductor quantum well. While, the QWIPs suffer from relatively low quantum efficiencies and lower operating temperatures, the excellent uniformity and lower cost offered by the gallium arsenide technology offers an important advantage for large focal plane arrays.

1.3 Figures of Merit for Infrared Detectors and Focal Plane Arrays

The most important figures of merit for infrared detectors and focal plane arrays are responsivity, detectivity, and noise equivalent temperature difference. In the following sections, these parameters will briefly be discussed.

1.3.1 Responsivity

Responsivity with the units of A/W or V/W is the ratio of detector's output signal to the incident radiant input. The output signal may be in the form of current or voltage. Naturally, a large responsivity is preferred for good sensitivity. However, responsivity is not the only figure of merit determining the sensitivity of an infrared sensor. Noise equivalent power or detectivity, as discussed in the following sections, define the sensitivity of an infrared sensor in a more comprehensive form.

1.3.2 Noise Equivalent Power

The noise equivalent power (NEP) is the detector noise referred to the optical input power or the optical input power that yields a unity signal-to-noise ratio at the output of a detector. NEP is defined as the ratio of detector noise to the responsivity of the detector.

1.3.3 Detectivity

Detectivity of a detector is defined as the reciprocal of NEP [2]:

$$D = \frac{1}{NEP} \quad 1/W \tag{1.3}$$

NEP and D both depend on the detector area and the bandwidth of the detection electronics. These dependencies yield different NEP and D values for detectors with different areas and for detection electronics with different bandwidths. Therefore NEP and D are not useful to compare different detectors. For this purpose, a new parameter called specific detectivity is defined as follows [2]

$$D^* = D\sqrt{A}\sqrt{\Delta\upsilon} \tag{1.4}$$

where A is the detector area (cm^2) and $\Delta\upsilon$ is the bandwidth of the detection electronics (Hz). If the detector response varies rapidly with the wavelength, then the specific detectivity is measured at a wavelength at which the detector yields the maximum response. Specific detectivity is the most important performance parameter for infrared detectors.

1.3.4 Noise Equivalent Temperature Difference (NETD)

Noise equivalent temperature difference (NETD) is the temperature change, for incident radiation, that gives an output signal equal to the rms noise level [7]. NETD is defined as follows [7]

$$NETD = V_n \frac{\Delta T}{\Delta V_s} \tag{1.5}$$

where V_n is the rms noise and ΔV_s is the signal measured for the temperature difference ΔT.

1.3.5 Time Constant

Time constant is defined as the time required for the detector output to reach 63% of its final value when an abrupt change is applied to the input. Time constant is designated as τ.

The above brief and general introduction will be continued with a summary of $Hg_{1-x}Cd_xTe$ detector technology in the following chapter.

CHAPTER 2

MERCURY CADMIUM TELLURIDE INFRARED DETECTORS AND FOCAL PLANE ARRAYS

$Hg_{1-x}Cd_xTe$ (mercury cadmium telluride) is an alloy of HgTe (mercury telluride) and CdTe (cadmium telluride). In $Hg_{1-x}Cd_xTe$, "x" and "1-x" indicate the mole fractions of CdTe and HgTe in the alloy, respectively. $Hg_{1-x}Cd_xTe$ has been the most important semiconductor for mid-wavelength and long-wavelength infrared imaging applications. After silicon (Si) and gallium arsenide (GaAs), $Hg_{1-x}Cd_xTe$ is the third most studied semiconductor material [8].

2.1 History of $Hg_{1-x}Cd_xTe$

The first detailed studies on $Hg_{1-x}Cd_xTe$ were reported by Lawson and colleagues in 1958 and 1959 [9]. They prepared $Hg_{1-x}Cd_xTe$ alloys with different CdTe and HgTe mole fractions. They saw that by changing the mole fractions it is possible to obtain $Hg_{1-x}Cd_xTe$ alloys with energy band gap values changing continuously from the energy band gap value of CdTe to that of HgTe [9]. They also reported the photoconductive and photovoltaic response of $Hg_{1-x}Cd_xTe$ alloys at wavelengths extending to 12 μm [10]. The 47-year history of $Hg_{1-x}Cd_xTe$ has seen the three generations of infrared detector devices namely the first, the second and

the third generations. The first generation of devices consists of photoconductive linear arrays, which have been produced in large quantities and are still in widespread use. The second generation devices consist of photovoltaic two dimensional arrays which are today in high production rate. The third generation devices are generally defined as more exotic detector structures such as two-color detectors, avalanche photodiodes, and hyper-spectral arrays, which are today far away from high volume production [11].

2.2 Material Related Issues

HgCdTe is the only well-behaved intrinsic semiconductor with an energy band gap of around 0.1 eV (for x ≈ 0.2), which makes this alloy very important for infrared imaging at LWIR band [8]. CdTe and HgTe have zinc-blende structures. $Hg_{1-x}Cd_xTe$, which is an alloy of HgTe and CdTe, has also zinc-blende structure for all x values. At 77 K, CdTe has an energy band gap value of 1.6088 eV and HgTe has an energy band gap value of –0.2608 eV. $Hg_{1-x}Cd_xTe$ has a direct energy band gap changing from energy band gap value of CdTe to that of HgTe as x varies from 1 to 0. There exist some equations expressing the energy band gap value of $Hg_{1-x}Cd_xTe$ in terms of x and temperature. The expression given by Seiler *et al.* is as follows [12]

$$E_g = -0.302 + 1.93x - 0.810x^2 + 0.832x^3 + 5.35\times10^{-4}(1-2x)\left(\frac{-1822 + T^3}{255.2 + T^2}\right) \quad (2.1)$$

where E_g is the energy band gap of $Hg_{1-x}Cd_xTe$ (eV), x is CdTe mole fraction (a scalar taking values between 0 and 1), and T is temperature (K). This equation should be applied to $Hg_{1-x}Cd_xTe$ with $0.17 < x < 0.30$. In Figure 2.1 energy band gap of $Hg_{1-x}Cd_xTe$ for CdTe mole fractions between 0.18 and 0.30 are given for three different temperatures with respect to Equation (2.1). Corresponding cut-off wavelengths can be calculated from the energy band gap values by using the simple expression given below

$$\lambda_{cut-off} = \frac{1.24}{E_g} \tag{2.2}$$

where $\lambda_{cut\text{-}off}$ is the cut-off wavelength of the material (μm), which indicates the upper wavelength limit that the material cannot absorb any photon, and E_g is the energy band gap of the material (eV). In Figure 2.2, cut-off wavelength of $Hg_{1-x}Cd_xTe$ as a function of CdTe mole fraction is given for three different temperatures. $Hg_{1-x}Cd_xTe$ has an adjustable energy band gap from 0.7 μm (x = 1) to 25 μm (x ≈0.18 at 77 K).

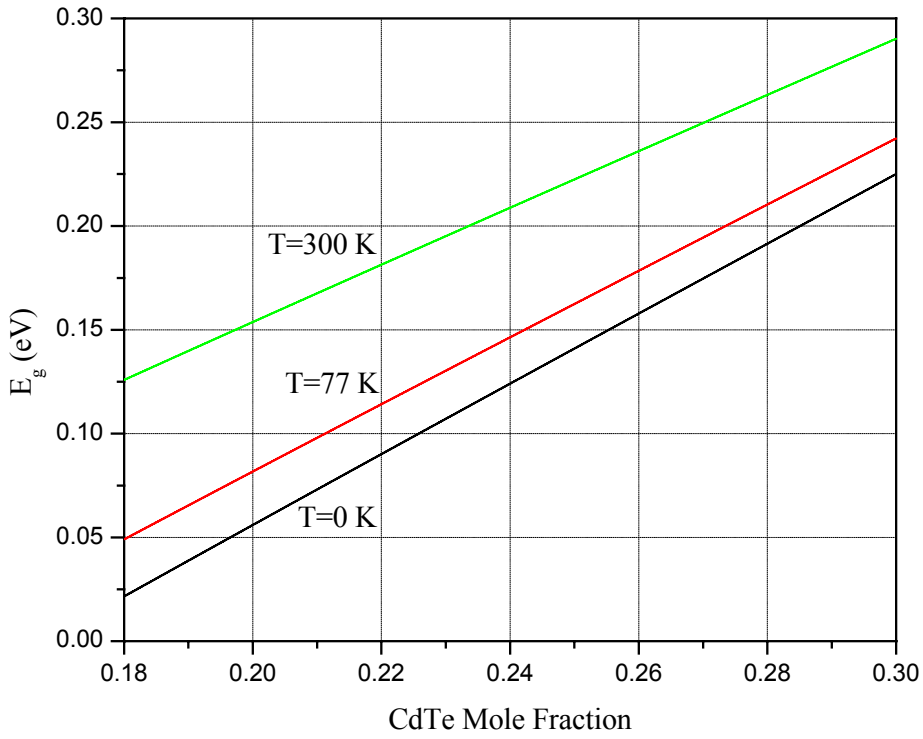

Figure 2.1: Energy band gap of $Hg_{1-x}Cd_xTe$ as a function of CdTe mole fraction for three different temperatures.

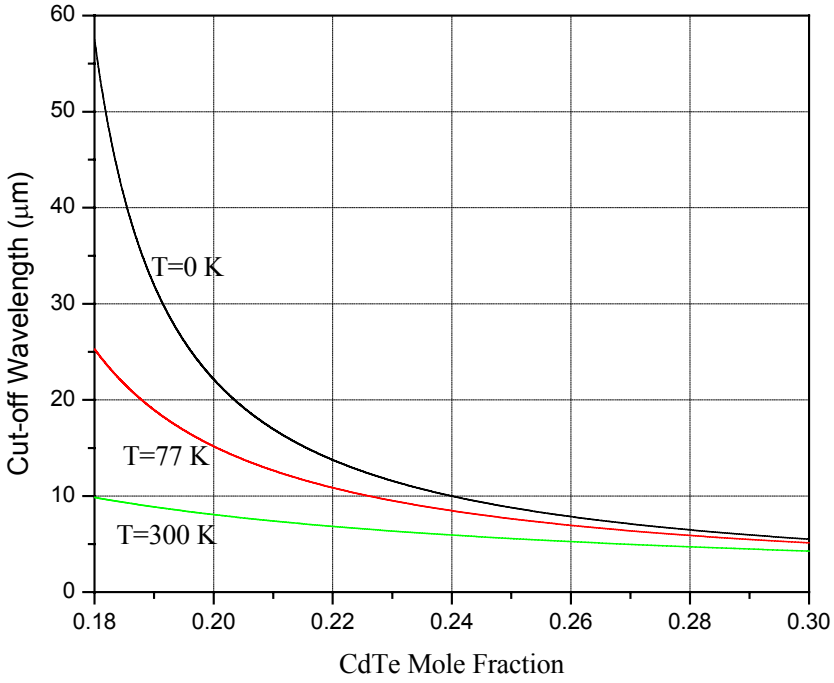

Figure 2.2: Cut-off wavelength of $Hg_{1-x}Cd_xTe$ as a function of CdTe mole fraction for three different temperatures.

The problem associated with large format LWIR $Hg_{1-x}Cd_xTe$ FPAs is well reflected by Figure 2.2. In The LWIR band (8-14 μm), the cut-off wavelength of $Hg_{1-x}Cd_xTe$ strongly depends on x (CdTe mole fraction), which results in considerable nonuniformity over a large area. Therefore, very large format LWIR staring FPAs are not available yet.

$Hg_{1-x}Cd_xTe$ is the unique semiconductor, which covers the entire infrared region of the electromagnetic spectrum with a small change in the lattice constant [8]. The lattice constant of $Hg_{1-x}Cd_xTe$ as a function of x is given by Higgins as follows [5]

$$a = 6.4614 + 0.0084x + 0.01168x^2 - 0.0057x^3. \qquad (2.3)$$

In Equation 2.3, "a" is in terms of angstroms (Å). The lattice constant of CdTe (x=1) is only 0.3% greater than that of HgTe (x=0). This is very important since small variation of lattice constant allows the fabrication of new devices based on lattice matched high quality complex heterostructures.

$Hg_{1-x}Cd_xTe$ is a direct energy band gap material, and it has a very sharp optical absorption characteristic. In Figure 2.3 optical absorption coefficient of $Hg_{1-x}Cd_xTe$ as a function of x is given [11]. As a result of the strong optical absorption of $Hg_{1-x}Cd_xTe$, relatively thin layer of $Hg_{1-x}Cd_xTe$ about 10–20 μm is sufficient for absorption of high percentage of the signal yielding high quantum efficiency.

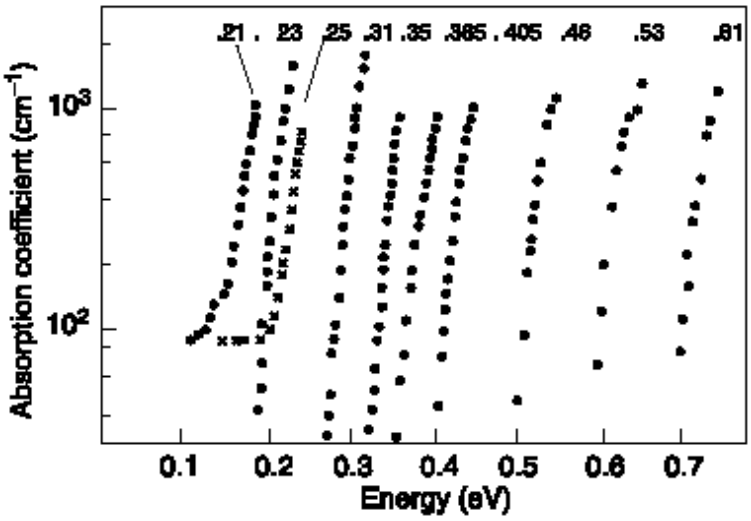

Figure 2.3: Optical absorption coefficient of $Hg_{1-x}Cd_xTe$ as a function of CdTe mole fraction [11].

2.3 $Hg_{1-x}Cd_xTe$ Growth

High quality epitaxial growth of $Hg_{1-x}Cd_xTe$ is required on a sufficiently large area for the fabrication of large format staring arrays. The standard substrate for HgCdTe is CdZnTe, which provides good lattice match with the HgCdTe epilayers. Liquid phase epitaxy (LPE), metal organic vapor phase epitaxy (MOVPE) or molecular beam epitaxy (MBE) technique can be utilized for the epitaxial growth of HgCdTe. While the conventional epitaxial growth technique

for HgCdTe is LPE, significant progress has been made on the growth of HgCdTe with MBE and MOVPE, which allow the fabrication of advanced and complex detector structures such as two-color detectors by providing good control of composition, layer thickness and doping. HgCdTe detector manufacturers have started to utilize MBE or MOVPE for the improvement of the detector performance and/or lower the cost of fabrication through the use of new detector structures and large Si or GaAs substrates. Articles and book chapters discussing the growth of HgCdTe with the above techniques in detail are available [13, 14]. More detailed discussion on the epitaxial growth of HgCdTe will be presented in the next chapter, which discusses the HgCdTe epitaxial layer structures used in this work.

2.4 $Hg_{1-x}Cd_xTe$ Infrared Detectors and Focal Plane Arrays

As mentioned above, $Hg_{1-x}Cd_xTe$ is a desirable material for infrared sensors due to its high quantum efficiency, tunable bandgap in a wide spectral region, and the ability to operate at moderately low sensor temperatures. Several $Hg_{1-x}Cd_xTe$ detector structures have been adopted by the $Hg_{1-x}Cd_xTe$ detector manufacturers and considerable amount of research work is carried out on the new structures. The most widely utilized $Hg_{1-x}Cd_xTe$ detector structures are described below.

2.4.1 Planar $Hg_{1-x}Cd_xTe$ Detectors

The first architecture used for hybrid $Hg_{1-x}Cd_xTe$ FPAs was backside illuminated planar n^+-p homojunctions. The absorber layer (p-type base layer) was grown by LPE. n^+-type cap layers were formed by ion implantation into the p-type base layer. This photodiode structure yielded an R_0A value of about 655 Ωcm^2 at 77 K for 10 μm cut-off wavelength. This R_0A value is close to the theoretical R_0A limit for the above wavelength [10].

2.4.2 Double Layer Heterojunction $Hg_{1-x}Cd_xTe$ Detectors

P-on-n (where capital P designates the wide energy band gap layer, and the lower case n designates the narrow energy gap layer) double layer heterojunction $Hg_{1-x}Cd_xTe$ photodiode structures became more popular than the planar n^+-p homojunctions due to the following advantages [10]:

- It is easier to control the low carrier concentration in n-type base layer than p-type base layer for $Hg_{1-x}Cd_xTe$,
- Passivation of n-type base layer is easier than p-type base layer,
- Lifetime of minority carriers in p-type $Hg_{1-x}Cd_xTe$ layers is limited due to Shockley-Read defects.

2.4.3 Loophole $Hg_{1-x}Cd_xTe$ Detectors

In this approach, $Hg_{1-x}Cd_xTe$ material is glued to the ROIC and then the substrate is thinned to 10-20 μm thickness. After the substrate thinning is performed, via holes are drilled to form electrical contacts between pixels of FPA with pixels of ROIC [10]. Figure 2.4 shows the loophole structure of $Hg_{1-x}Cd_xTe$ detectors.

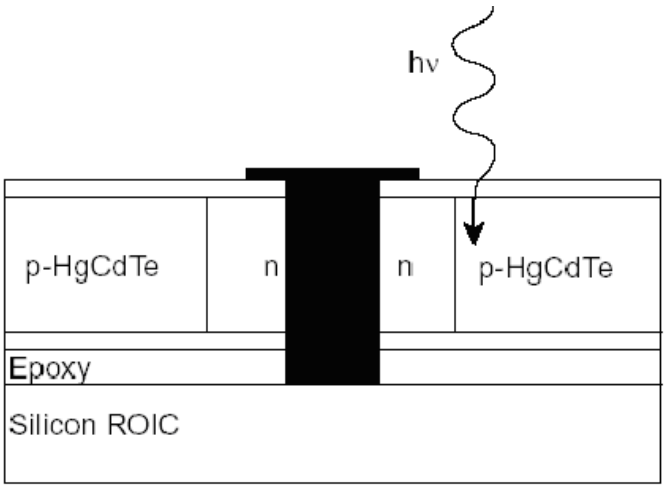

Figure 2.4: Loophole detector structure [10].

2.5 Comparison of Alternative Technologies

InSb and $Hg_{1-x}Cd_xTe$ have been the standard materials for MWIR detectors, and very large format arrays (1024x1024 or 2048x2048) have been reported for both technologies [15], [16]. Since InSb is a binary compound, the compositional uniformity is not an issue. However, InSb forces to use relatively low sensor temperatures due to approximately ten times higher trap density and fixed energy bandgap (λ_c=5.5 μm) [7], which does not allow tuning of the detector to operate with the desired cut-off wavelength.

Due to the difficulty of growing LWIR $Hg_{1-x}Cd_xTe$ over large area, alternative LWIR materials such as InAsSb, InSbBi, InAsBi, InAsSbBi, GaInSbBi, InTlSb, and InTlAs [17, 18, 19] have long been studied. However, these materials have not matured to the level of large format FPA fabrication yet.

The most promising alternative for $Hg_{1-x}Cd_xTe$ in the LWIR band appeared with the utilization of multi-quantum well structures for infrared detection (QWIP). In a QWIP, photo-generation occurs through the excitation of bound electrons in a quantum well to the continuum. Since the photo-excitation does not occur across the fundamental energy band gap of the semiconductor, relatively large band gap semiconductor systems with mature technologies (such as AlGaAs/GaAs) can be utilized to detect infrared radiation. The most important advantages of the QWIP technology are excellent uniformity, reproducibility, and significantly lower cost of fabrication. However, relatively low quantum efficiency of QWIP is still a bottleneck. There is considerable debate going on the comparison of QWIP and $Hg_{1-x}Cd_xTe$ detectors. However, there seems to be no doubt that $Hg_{1-x}Cd_xTe$ offers better sensitivity, especially under low background conditions, when the two detectors are compared at a single pixel level. The excellent uniformity offered by the QWIP technology allows large format QWIP FPAs offering NETDs similar to those of $Hg_{1-x}Cd_xTe$ FPAs [20].

When the $Hg_{1-x}Cd_xTe$ and QWIP technologies are compared for two-color or multi-color detection, QWIPs offer the advantages of easier growth and fabrication of complex epilayer structures and narrow-band spectral response, which allows the isolation of different colors.

There is significant amount of work being reported for higher performance LWIR thermal imaging through the improvement of QWIP performance. However, it seems that $Hg_{1-x}Cd_xTe$ will remain as an unavoidable material for infrared detection for a long time, if not forever.

2.6 State of the Art $Hg_{1-x}Cd_xTe$ FPAs

As discussed above, while very large format staring FPAs are feasible with $Hg_{1-x}Cd_xTe$ in the MWIR band, linear scanning arrays seems to be the only choice for very high resolution thermal imaging in the LWIR band, at least in the near future. The format of the state of the art HgCdTe FPAs are 1024x1024 for MWIR staring arrays and 576x7 for LWIR scanning arrays, respectively. LETI has recently reported a very large format (1024×1024) MWIR $Hg_{1-x}Cd_xTe$ FPA [16] with an NETD of 20 mK at 77 K. Sofradir demonstrated several LWIR $Hg_{1-x}Cd_xTe$ staring FPAs with a maximum format of 384x288 yielding NETD values around 15 mK with f/2 optics. [21]. Recently, Rockwell Scientific Company reported a 512×512 LWIR $Hg_{1-x}Cd_xTe$ FPA with 9.6 μm cut-off wavelength [22].

Current research work on $Hg_{1-x}Cd_xTe$ FPAs is concentrated on multi-color FPAs, detector quality growth on alternative substrates such as Si and GaAs, and large format LWIR staring array FPAs.

This chapter has presented the potential of $Hg_{1-x}Cd_xTe$ as an infrared sensor material. Next chapter describes and discusses the $Hg_{1-x}Cd_xTe$ epilayer structures used in this work for the fabrication of LWIR staring array FPAs.

CHAPTER 3

MERCURY CADMIUM TELLURIDE EPILAYER STRUCTURES

$Hg_{1-x}Cd_xTe$ epilayers that are used in this study are grown by MOVPE method. Epitaxial growth of $Hg_{1-x}Cd_xTe$ becomes more popular than bulk growth methods, since epitaxial growth offers larger area $Hg_{1-x}Cd_xTe$ wafers and allows the growth of sophisticated detector structures with abrupt and complex composition (CdTe mole fraction) and doping profiles. Other advantages of epitaxial growth are the lower growth temperature and the lower mercury pressure, which makes the growth environment easier to control.

Epitaxial growth of $Hg_{1-x}Cd_xTe$ epilayers requires substrates on which epilayers are grown. Substrates should be available in suitably large dimensions, and should be lattice matched to the epilayers, otherwise the epilayer quality would be poor. The substrate should preferably be a large energy band gap material so that it does not absorb the desired infrared radiation for backside-illuminated applications. Initially, CdTe was used as substrate for the epitaxial growth of $Hg_{1-x}Cd_xTe$. CdTe is an appropriate semiconductor as an infrared detector substrate, since it is transparent out to 30 μm, which allows backside illumination of the detector. Also CdTe does not act as a dopant for the epitaxial $Hg_{1-x}Cd_xTe$ layer. Finally, even CdTe is not as robust as Si or GaAs, it is still not as fragile as $Hg_{1-x}Cd_xTe$. The

main disadvantage of CdTe as a substrate for epitaxial growth of $Hg_{1-x}Cd_xTe$ is its lattice mismatch with MWIR and LWIR $Hg_{1-x}Cd_xTe$. In order to solve this problem, $Cd_{1-z}Zn_zTe$ (Cadmium Zinc Telluride) substrates with Zn concentration z=0.04 have widely been used for the epitaxial growth of $Hg_{1-x}Cd_xTe$. Besides CdZnTe, there also exist other lattice matched substrates for $Hg_{1-x}Cd_xTe$ such as CdTeSe (Cadmium Tellur Selenide) and CdMnTe (Cadmium Manganese Telluride). However CdTeSe and CdMnTe have purity problems [13]. Sapphire is another substrate that can be used for $Hg_{1-x}Cd_xTe$ epitaxy. However, since sapphire has a large lattice mismatch with $Hg_{1-x}Cd_xTe$, buffer layer growth before the $Hg_{1-x}Cd_xTe$ epitaxy is mandatory. Since sapphire is transparent only from UV to 6 μm, it cannot be used for backside illuminated LWIR $Hg_{1-x}Cd_xTe$ detectors. Germanium, gallium arsenide and silicon are also used as substrate for $Hg_{1-x}Cd_xTe$ epitaxy. LWIR, MWIR, and SWIR $Hg_{1-x}Cd_xTe$ detectors can be fabricated on Ge, GaAs, and Si substrates, if the problems arising from large lattice mismatch can be eliminated. CdTe buffer layers are necessary before the $Hg_{1-x}Cd_xTe$ epitaxy for this purpose. In the next section, the epilayer structures used in this work and design considerations will be described.

3.1 Epilayer Structures and Design Considerations

In Figure 3.1, $Hg_{1-x}Cd_xTe$ epilayer structures that are used in this thesis study are given. All the three structures shown in Figure 3.1 are p-on-n $Hg_{1-x}Cd_xTe$ epilayer structures grown on lattice matched CdZnTe substrates by MOVPE at QinetiQ Inc.

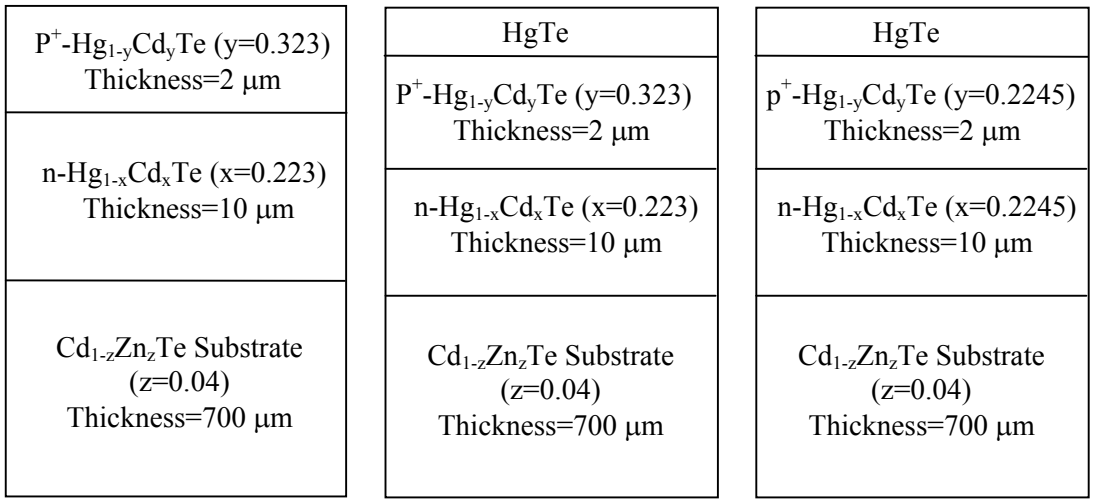

Figure 3.1: $Hg_{1-x}Cd_xTe$ epilayers that are designed and used for test detector and FPA fabrication in this study: (a) & (b) Structure 1, (c) Structure 2.

3.1.1 Structure 1

The structures shown in Figure 3.1 (a) and (b) are basically the same structures except the one in (b) is ex-situ HgTe deposited by an MOVPE system. Both structures are designed to be double layer heterostructures with x<y, where the P-type $Hg_{1-x}Cd_xTe$ layer has a larger energy band gap than the n-type $Hg_{1-x}Cd_xTe$ layer. Substrate of Structure 1 is CdZnTe lattice matched to the n-type $Hg_{1-x}Cd_xTe$. Thickness of the substrate is about 700 μm and the dimensions are 20 mm x 20 mm. The backside of the substrate is polished.

The n-type $Hg_{1-x}Cd_xTe$ layer is called the "bottom layer" in the following parts of this thesis. The bottom layer is the active layer of this detector structure that absorbs the desired infrared radiation. Therefore, CdTe mole fraction of this layer must be adjusted so that the energy band gap of the epilayer is set to the desired infrared wavelength. The CdTe mole fraction of the bottom layer is selected to be 0.223. This composition value corresponds to cut-off wavelength of 10.4 μm at 77 K, which can be calculated by using Equations (2.1) and (2.2). By considering the absorption coefficient and the diffusion length, thickness of the bottom layer is optimized to get near 100% quantum efficiency. Thickness is set to a value

slightly larger than the inverse of the absorption coefficient of $Hg_{1-x}Cd_xTe$, namely $1/\alpha$, which is about 10 μm for x=0.223. This thickness is smaller than the diffusion length so that almost all of the carriers photo-generated in the bottom layer can be collected by the electrical junction [23, 24]. The bottom layer is in-situ doped with Iodine at a level of $1–3x10^{15}$ cm^{-3}, which is the lowest possible n-type doping for $Hg_{1-x}Cd_xTe$ by MOVPE growth. The doping level is preferred to be as low as possible in order to decrease the recombination in the bottom layer and keep the quantum efficiency high [23]. The electrical junction must be located in the narrow band gap layer in order not to decrease the quantum efficiency of the detector. Otherwise, the resulting barriers reduce the quantum efficiency [25, 26, 27, 28].

The P-type $Hg_{1-x}Cd_xTe$ layer is called the "top layer" in the following parts of this thesis. Structure 1 is designed as a double layer heterojunction, and the CdTe mole fraction of the top layer is set to y=0.323 [1, 25, 29-32]. Thermal generation rate in the top layer is lower than that in the bottom layer because of the large energy band gap. The top layer is in-situ doped with Arsenic at a level of $1–3$ $x10^{17}$ cm^{-3}, which is the highest possible p-type doping level for $Hg_{1-x}Cd_xTe$ by MOVPE. The high p-type doping level results in low electron concentration in the top layer. As a consequence, dark current from the top layer is kept at a sufficiently low level. The thickness of the top layer is designed to be 2 μm. This layer is kept to be thin in order not to increase the dark current [30].

The structure given in Figure 3.1 (b) has an additional HgTe layer on the P-type $Hg_{1-x}Cd_xTe$ layer. This layer is ex-situ deposited by an MOVPE system, after our study on the formation of good ohmic contacts on this layer using alternative techniques have failed. It is generally difficult to establish ohmic contacts on p-type doped $Hg_{1-x}Cd_xTe$. In order to form ohmic contacts on p-type $Hg_{1-x}Cd_xTe$, a high work function metal is necessary. HgTe is a high workfunction semi metal, and it is reported to form ohmic contacts on p-type $Hg_{1-x}Cd_xTe$ [33].

In Table 3.1 some of the properties of $Hg_{1-x}Cd_xTe$ samples used in this study are given. In Figures 3.2, 3.3, and 3.4, Fourier Transform Infrared (FTIR) spectroscopy maps of n-type $Hg_{1-x}Cd_xTe$ layers of the samples are shown. These maps have been supplied by QinetiQ Inc. These maps show the CdTe mole fraction uniformity of the n-type $Hg_{1-x}Cd_xTe$ layers.

Table 3.1: Some of the properties of $Hg_{1-x}Cd_xTe$ samples that are used during this study.

Sample	**Structure**	**x**	**$\lambda_{cut-off}$ (μm)**
K712	Structure 1(a)	0.2151±0.0010	11.67
JE02	Structure 1(b)	0.2196±0.0011	10.92
K714	Structure 1(b)	0.2136±0.0011	11.94
G511	Structure 2	0.2245±0.0011	10.21

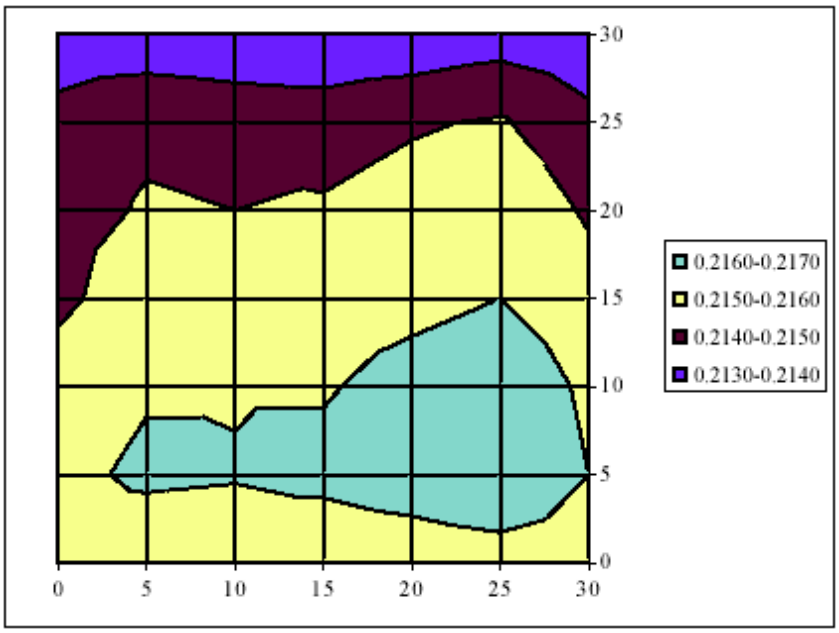

Figure 3.2: FTIR map of sample K712

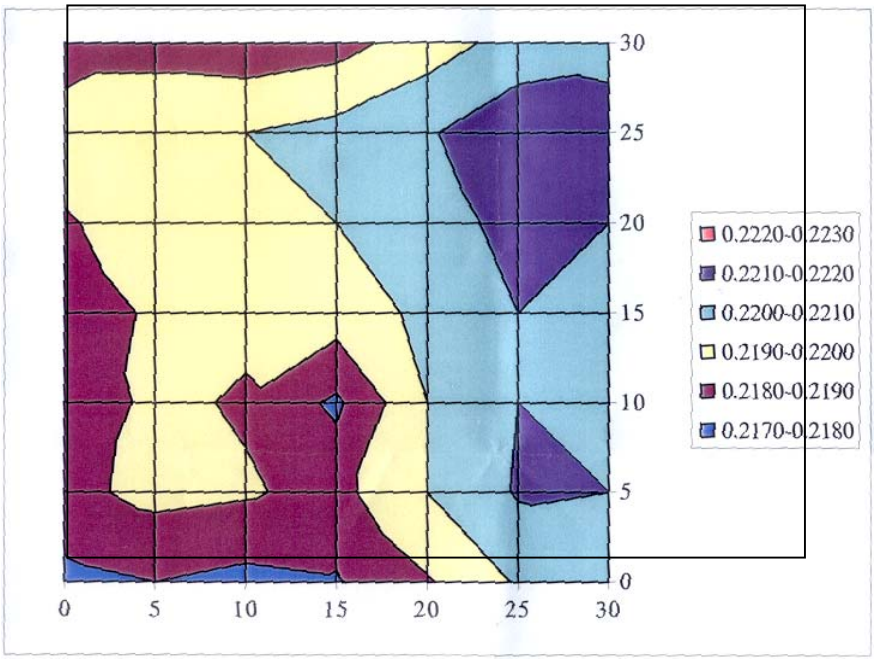

Figure 3.3: FTIR map of sample JE02

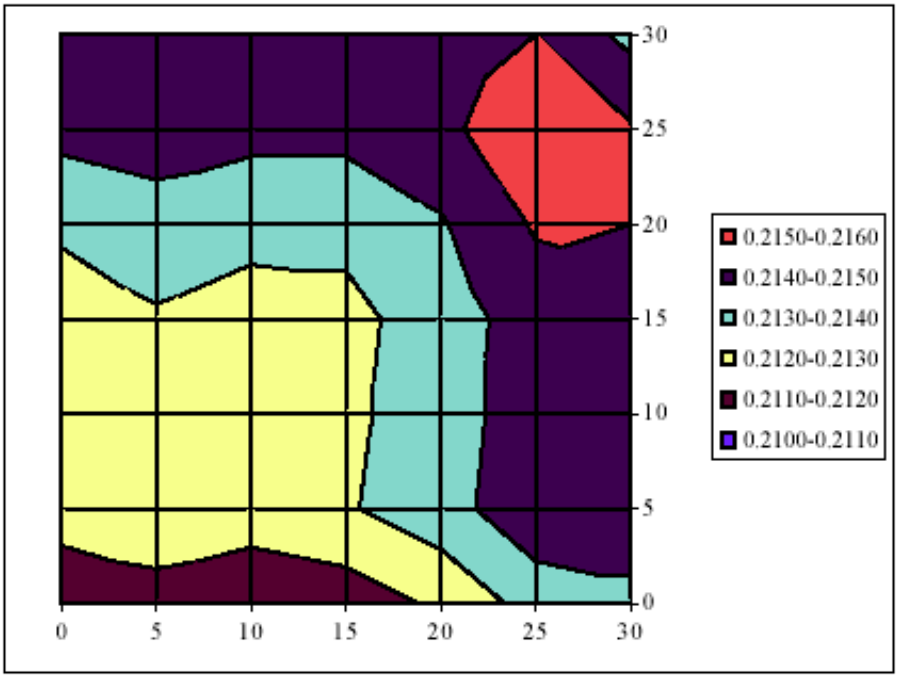

Figure 3.4: FTIR map of sample K714

3.1.2 Structure 2

While the $Hg_{1-x}Cd_xTe$ detector structure given in Figure 3.1 (c) is similar to the structures in Figure 3.1 (a) and (b), there are two main differences; Structure 2 is a homojunction layer whereas Structure 1 is a heterojunction structure, and Structure 2 is in-situ HgTe deposited whereas Structure 1 (b) is ex-situ HgTe deposited. Since this structure is a homojunction, n-type and p-type $Hg_{1-x}Cd_xTe$ layers have the same CdTe mole fraction. Substrate of Structure 2 is CdZnTe with dimensions of 20 mm x 20 mm and thickness of 700 μm. The CdTe mole fraction of bottom and top layers of the Structure 2 is set to x=0.223 to tune the cut-off wavelength at 10.4 μm. The bottom layer is in-situ doped with Iodine at a level of $1–3x10^{15}$ cm^{-3}. The top layer is in-situ doped with Arsenic to a level of $1–3$ $x10^{17}$ cm^{-3}. Thickness of the bottom layer is 10 μm, and thickness of the top layer is 2 μm. These doping concentration and thickness values were determined with similar design criteria as explained above in Section 3.1. In Table 3.1 some of the properties of $Hg_{1-x}Cd_xTe$ sample with Structure 2 are given.

3.2 Comparison of n^+-on-p and p^+-on-n Detector Structures

Theoretical analysis predicts that an $Hg_{1-x}Cd_xTe$ photodiode with a lightly doped p-type bottom layer and degenerately doped or wide gap n-type top layer has the highest performance. However, it is not easy to obtain sufficiently low doping concentration in the p-type $Hg_{1-x}Cd_xTe$ material, since the control of hole concentration below 10^{16} cm^{-3} is very difficult in $Hg_{1-x}Cd_xTe$. Also p-type $Hg_{1-x}Cd_xTe$ has non-fundamental limitations such as bad ohmic contacts, and performance degrading surface and Shockley-Read recombination processes [34]. On the other hand, it is possible to obtain n-type doping concentration in $Hg_{1-x}Cd_xTe$ as low as $10^{14}–10^{15}$ cm^{-3} resulting in longer minority carrier lifetimes [35].

In Figure 3.5 (a), R_0A product of a homojunction n^+-on-p $Hg_{1-x}Cd_xTe$ (x=0.21) photodiode is given as a function of the electrical junction depth. The influence of the n^+ layer thickness on the R_0A product is important if the electrical junction

depth is below 0.2 μm. This is not an unexpected result since the minority carrier diffusion length in n^+-type $Hg_{1-x}Cd_xTe$ is about 0.2 μm. The dashed line in Figure 3.5 (a) gives the calculated R_0A product by considering only the thermal generation in the p-type bottom layer [35]. Since Auger 7 mechanism dominates the generation-recombination processes in high quality p-type $Hg_{1-x}Cd_xTe$, the dashed line represents the maximum R_0A value possible for an n^+-on-p $Hg_{1-x}Cd_xTe$ photodiode [5]. In Figure 3.5 (b), R_0A product of a homojunction p^+-on-n $Hg_{1-x}Cd_xTe$ photodiode is given as a function of the junction depth. R_0A product for p^+-on-n junction is about 10 Ωcm^2 for junctions deeper than 1 μm. The dashed line in Figure 3.5 (b) gives the calculated R_0A product by considering only the thermal generation in the n-type bottom layer, which is equal to 160 Ωcm^2. Since Auger 1 mechanism dominates the generation-recombination processes in high quality n-type $Hg_{1-x}Cd_xTe$, the dashed line represents the maximum R_0A value possible for a p^+-on-n $Hg_{1-x}Cd_xTe$ photodiode [5]. In order to avoid the negative influence of the p^+ $Hg_{1-x}Cd_xTe$ layer on the photodiode performance, it is mandatory to design the top layer as a wide gap layer. The wide gap top layer has also other positive influences on the photodiode performance such as lower generation-recombination noise in heterojunction P^+-on-n $Hg_{1-x}Cd_xTe$ photodiodes [12]. In the case of P^+-on-n $Hg_{1-x}Cd_xTe$, the narrow gap n-type bottom layer is sandwiched between wider band gap regions, namely CdZnTe substrate and wide gap P^+-$Hg_{1-x}Cd_xTe$ top layer to suppress negative influence of contacts and the p-type layer.

This chapter has discussed the $Hg_{1-x}Cd_xTe$ epilayers and design considerations of this work. The development of LWIR $Hg_{1-x}Cd_xTe$ FPA fabrication process will be described in the next chapter.

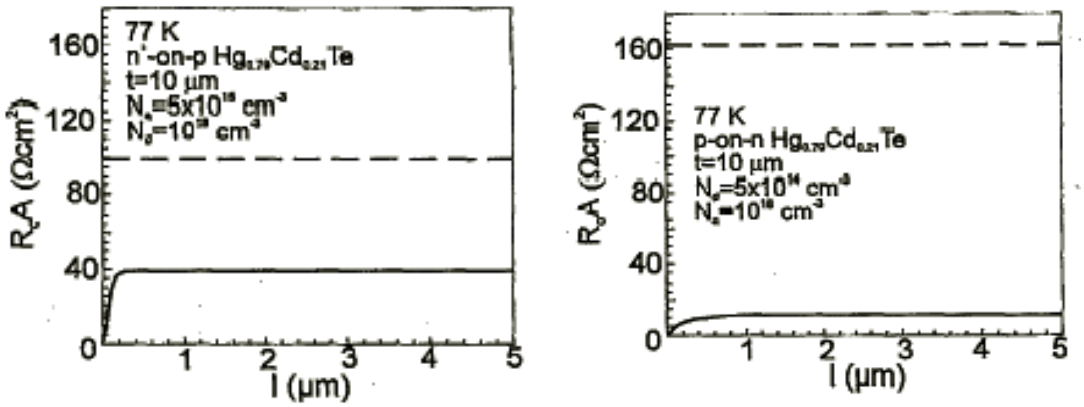

(a) (b)

Figure 3.5: R_0A product as a function of junction depth for n^+-on-p $Hg_{1-x}Cd_xTe$ (x=0.21) (a) and p^+-on-n $Hg_{1-x}Cd_xTe$ (x=0.21) (b). The dashed lines represent the maximum possible R_0A product [35].

CHAPTER 4

DEVELOPMENT OF FOCAL PLANE ARRAY FABRICATION PROCESS AND 128x128 MERCURY CADMIUM TELLURIDE FOCAL PLANE ARRAY FABRICATION

Infrared FPA fabrication is a complicated process consisting of a number of steps that must be properly optimized. In this thesis study, fabrication process of 128x128 $Hg_{1-x}Cd_xTe$ FPAs was developed. In the following sections of this chapter, this study will be described in detail.

In order to give an idea about the final structure of the fabricated FPA, we show in Figure 4.1 the picture of the 128x128 HgCdTe FPA after the hybridization with the read-out integrated circuit (ROIC) is completed. After fabricating the detector array, the pixels of the array are aligned with those of the ROIC, and the detector array is flip-chip bonded to the ROIC. Each pixel of the detector array is connected to the corresponding pixel of the ROIC through small indium bumps, which are formed on both the detector array and the ROIC before hybridization.

The detector array is illuminated from the backside. The CdZnTe substrate, which is transparent in the LWIR band, transmits the infrared radiation with negligible absorbance to the pixels of the detector array. The photocurrent generated by each

pixel of the detector array is read by the corresponding pixel of the ROIC, and the signals generated by the pixels of the FPA is sent out serially through a pin of the ROIC as analog signals. The signals coming out of the ROIC are fed into external electronic circuits for processing, forming the thermal image and displaying it on a monitor. The ROIC (ISC 9806) adopted in this study is supplied by Indigo systems, and it is a commercial ROIC optimized for QWIP and InSb detectors. The basic properties of the ROIC are given in Table 4.1 [36].

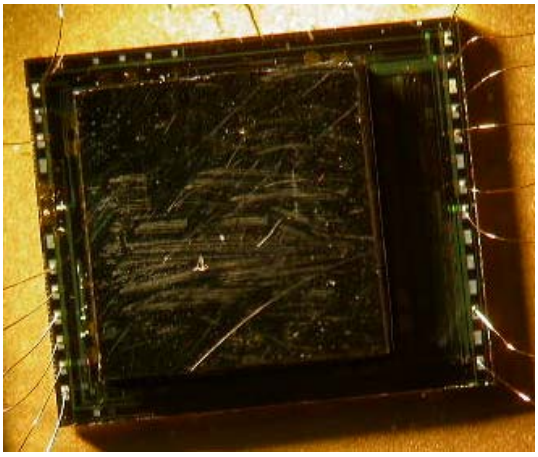

Fig. 4.1 Fabricated 128x128 HgCdTe FPA

Table 4.1: Technical specifications of ISC9806 ROIC [36].

Format	128x128
Pixel Pitch	38 µm
Storage Capacity	3.5×10^7 electrons
Input Current	0.02 nA (min.), 1 nA (typ.), 10 nA (max.)
Readout Noise	500 electrons
Input Polarity	p on n
Integration Time	>6 µsec, adjustable
Outputs	1, 2, or 4 selectable
Power Consumption	<90 mW at 30 Hz single output <180 mW at 107 Hz, 4 outputs
Max Frame Rate at 80 K	15600 Hz
Video Output	NTSC or PAL

4.1 128x128 $Hg_{1-x}Cd_xTe$ FPA Fabrication Steps

Before presenting the details of the fabrication process, the stages of the FPA process are listed below with the purpose of each step.

i. **Metal deposition for alignment marks:** This step is necessary for aligning the wafer with the pattern on the mask during processing.
ii. **Mesa etch:** The purpose of this step is the definition of the detector array pixels by etching and isolating them from each other.
iii. **Metal deposition for ohmic contacts:** This step is necessary for good electrical connection to each photodiode on the array.
iv. **Passivation material deposition:** The purpose of this step is reducing the dark current of the detectors and improving the detector performance by passivating the surfaces of the detector array pixels. The passivation material deposited in this process also protects the surface of the detector material.
v. **Under bump metallization:** This step is implemented to provide the metallization on the detector array pixels, which allows reliable In bumps.
vi. **Indium electroplating:** In this step, small In bumps (with a diameter of around 10 μm) are uniformly formed on the pixels of the detector array and ROIC separately. In bumps are necessary for connecting the pixels of the detector array to the pixels of the ROIC.
vii. **Dicing of FPA**
viii. **Hybrid coupling of FPA and ROIC by flip-chip bonding:** In this process, the detector array pixels are aligned with the pixels of the ROIC and the hybridization is implemented with an optimized process.
ix. **Underfill epoxy injection and curing:** The gap between the detector array and the ROIC (< 10 μm) is completely filled with an epoxy to provide mechanical strength.

x. **Substrate lapping and polishing:** This process is necessary for increased strength of the FPA against thermal cycles, as well as for reducing the optical cross talk between the pixels of the FPA. However, this step is not optimized in this work.

$Hg_{1-x}Cd_xTe$ is a mechanically very fragile and sensitive material due to the weak nature of Hg–Te bonds [1]. Furthermore, exposing the material to temperatures higher than 80°C degrades the properties of the material. Therefore, $Hg_{1-x}Cd_xTe$ is not an easy material to process for device fabrication. In this work, necessary precautions were taken during processing not to degrade the material properties.

The following sections describe the study toward the optimization of mesa etch and ohmic contact which differ from the processes of other infrared material due to some unique properties of HgCdTe. The other steps of the fabrication will be presented without going into the details.

4.1.1 Mesa Etch Study

The size of ISC9806 unit cell determines the size of pixel pitch of FPA, which is 38 μm. Each mesa has the dimensions of 33x33 μm^2 and is separated from its neighbors by 5 μm. Mesa etching must yield uniform etch depth across the FPA. Besides etch depth uniformity, underetch amount is also important. Mesa etching should cause a reasonable amount of underetch, since underetch reduces the fill factor of detector pixels which means reduction in the detector area absorbing the infrared radiation.

There exist different methods to etch $Hg_{1-x}Cd_xTe$ such as wet etch, plasma etch, and ion beam milling (IBM). There are various plasma etch methods which differ in plasma activation: parallel plate radio frequency in reactive ion etching (RIE), microwave electron cyclotron resonance (ECR), or a hybrid technique including both ECR and RIE. Methane (CH_4) and hydrogen (H_2) plasma is preferred for etching $Hg_{1-x}Cd_xTe$. Plasma etch provides very sharp mesa profiles with very low

underetch. However, due to the weak nature of Hg–Te bonds, plasma etch results in type conversion in this material: p-type $Hg_{1-x}Cd_xTe$ becomes n-type $Hg_{1-x}Cd_xTe$, and n-type $Hg_{1-x}Cd_xTe$ becomes n^+-type $Hg_{1-x}Cd_xTe$. Besides type conversion, plasma etch also causes a change in the stoichiometric composition, and it results in surface roughness and polymer deposition. In order to restore the original conductive mode and carrier concentration in the affected region, etched sample should be annealed in saturated Hg vapor at 150–200ºC in a sealed quartz ampoule. The type conversion and its reversibility are assumed to be correlated with the in-diffusion and out-diffusion of atomic hydrogen. It is thought that atomic hydrogen forms complexes with acceptor atoms and neutralizes them. These complexes seem to be stable at temperatures lower than 100ºC [37, 38].

In the IBM process, low energy argon ions (100-1000 eV) are used. IBM process creates a high density of defects in $Hg_{1-x}Cd_xTe$. Similar to RIE, IBM process also causes type conversion in $Hg_{1-x}Cd_xTe$ [38]. On the other hand, wet etching does not cause any type conversion; however it may result in considerable underetch.

In this work, wet etching technique is adopted for the formation of the detector mesas. In order to determine the best solution among the alternatives, several wet etch solutions are investigated. These solutions are listed below.

- Br_2/HBr [39]
- HF/H_2O_2/H_2O
- Br_2/Ethylene Glycol [40]
- HCl/HNO_3/H_2O

Even though methanol-containing etch solutions also exist such as (Br_2/Methanol and HBr/Methanol), these solutions were not examined due to the photoresist mask, which is destroyed by methanol. Due the high cost and small quantity of the material used in this study, small (5 mm x 5 mm) pieces of wafers were utilized during the wet etch study. Figure 4.2 shows the etch study pattern

designed in this work. In the first part of the study, only the right side of the sample is used. Number labels 1, 2, 3, and 4 represent the sample areas on which four different solutions were applied. In the second part of the etch study, the selected solution is used to etch the mesa patterns of FPA. This is done on the left side of the sample. Br_2/HBr was applied to region 1, $HF/H_2O_2/H_2O$ was applied to region 2, Br_2/Ethylene Glycol was applied to region 3, and finally $HCl/HNO_3/H_2O$ was applied to region 4. Etch durations are given in Table 4.2. All the etching processes were carried out at 25ºC by stirring the etch solution at 300 rpm.

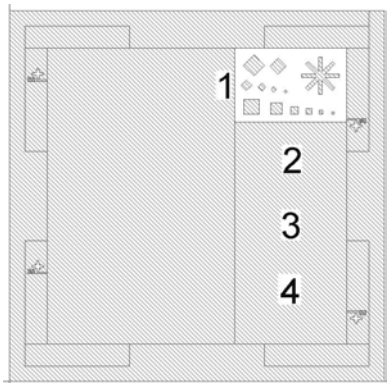

Figure 4.2: One of the masks used during etch optimization.

Table 4.2: Etch solutions and corresponding etch durations

Etch Solution	**Etch Duration (seconds)**
Br_2/HBr	45
$HF/H_2O_2/H_2O$	20 + 180
Br_2/Ethylene Glycol	5 + 90 + 80 + 80 + 30
$HCl/HNO_3/H_2O$	20 + 50

In Figure 4.3, photographs taken by an optical microscope of the etched surfaces are given. Figure 4.3 (a) corresponds to region 1, Figure 4.3 (b) corresponds to region 2, Figure 4.3 (c) corresponds to region 3, and finally Figure 4.3 (d) corresponds to region 4. As it can be seen from Figure 4.3 (b) and (d), $HF/H_2O_2/H_2O$ and $HCl/HNO_3/H_2O$ solutions are not appropriate, since they leak

under photoresist and etched the regions protected by photoresist. Br_2/Ethylene Glycol solution does not etch the surface uniformly. Especially the south part of the sample was etched deeper than the remaining parts, which can be seen in Figure 4.3 (c). This was verified by surface profiling measurements. Figure 4.3 (a) shows the region etched by Br_2/HBr. This solution etches the surface uniformly without attacking the photoresist and the regions protected by photoresist. The defects were caused by deformations formed on the photoresist.

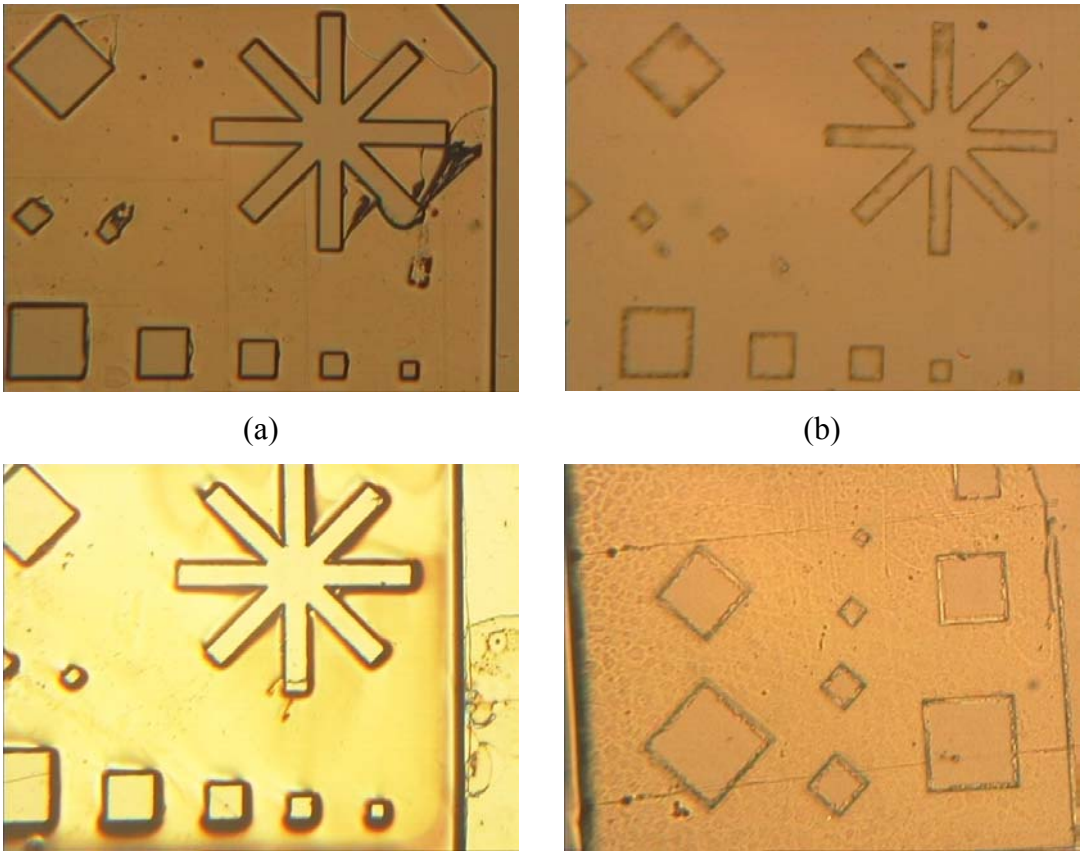

(a) (b)

(c) (d)

Figure 4.3: Sample regions etched with different solutions: (a) is etched by Br_2/HBr, (b) is etched by $HF/H_2O_2/H_2O$, (c) is etched by Br_2/Ethylene Glycol, and (d) is etched by $HCl/HNO_3/H_2O$.

Etched regions shown in Figure 4.3 were also investigated with a Scanning Electron Microscope (SEM). Photographs taken by SEM are given in Figure 4.4. In Figure 4.4 (a) from left to right, regions 1 (etched with Br_2/HBr), 2 (etched with $HF/H_2O_2/H_2O$), and 3 (etched with Br_2/Ethylene Glycol) are shown. In

Figure 4.4 (b) from left to right, regions 2 (etched with $HF/H_2O_2/H_2O$), and 3 (etched with Br_2/Ethylene Glycol), and 4 (etched with $HCl/HNO_3/H_2O$) are shown. The problems with solutions $HF/H_2O_2/H_2O$, Br_2/Ethylene Glycol, and $HF/H_2O_2/H_2O$ can be also seen very easily from the SEM pictures. Even though region 2 is etched for 200 seconds, it does not have a significant etch depth nevertheless etch solution destroys photoresist and etches the regions protected by photoresist. Region 4 has the similar problem as region 2. Region 3 is etched nonuniformly which is evident from Figure 4.4 (b).

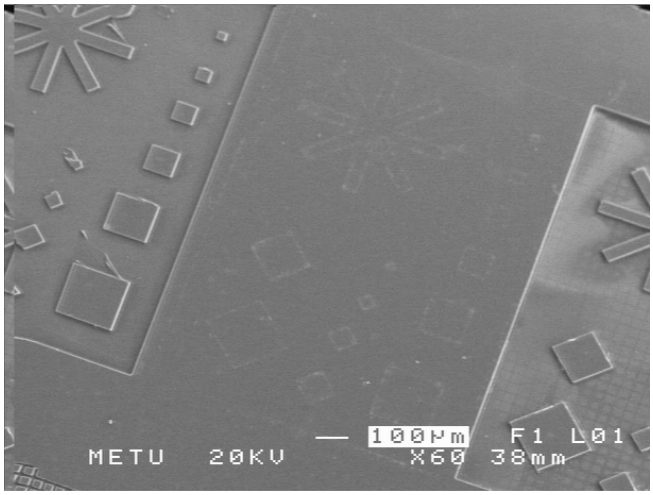

(a)

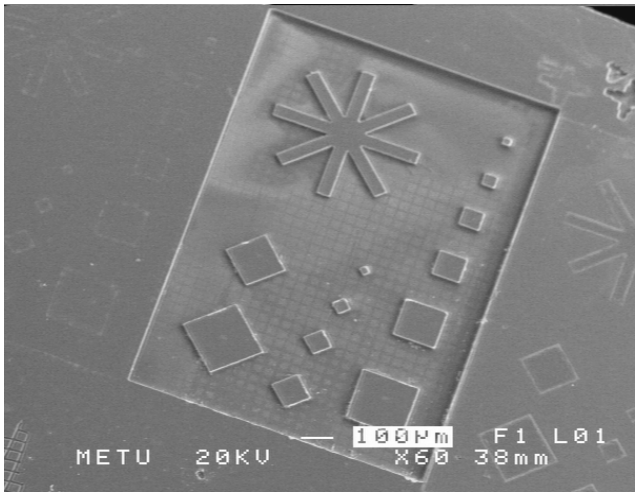

(b)

Figure 4.4: SEM pictures of etched regions: (a) from left to right regions 1, 2, and 3; (b) from left to right regions 2, 3, and 4.

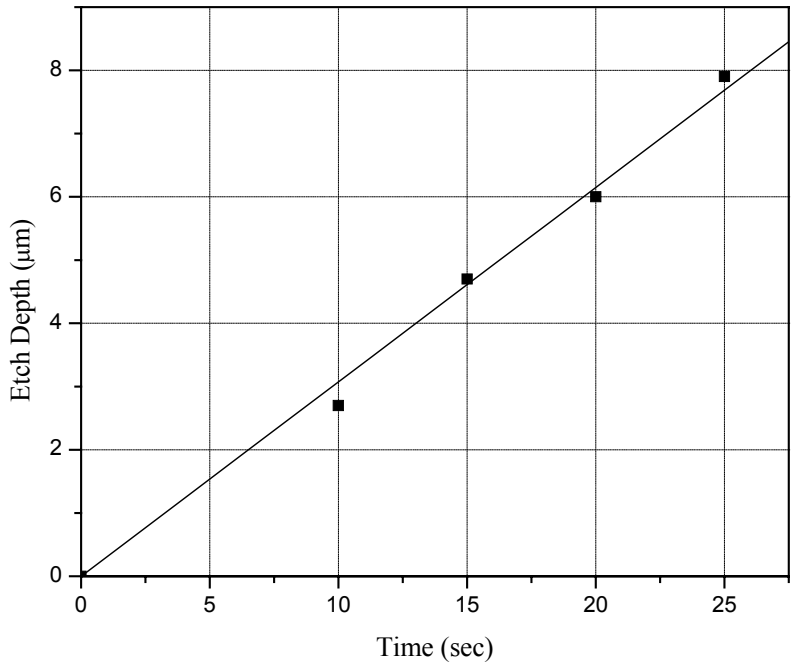

Figure 4.5: Etch rate of Br_2/HBr solution.

Br_2/HBr solution was selected for further investigation as a potential etch solution for the FPA fabrication process, since it yielded acceptable results. First of all, the etch rate of this solution was determined. Figure 4.5 presents the results of this study.

After determining the etch rate, the left part of the sample was used in the next part of the etch study in order to investigate the performance of Br_2/HBr solution during mesa etch of FPA fabrication process. The SEM and optical microscope photographs given in Figure 4.6 correspond to different etch durations. The photographs in Figures 4.6 (c) and (d) are taken by SEM on the opposite sides of the sample. Etch duration is 10 seconds for both photographs. These two photographs indicate the etch uniformity. Etch depth is around 2.5 μm which is consistent with the etch rate determined in the previous step. In Figures 4.6 (e) and (f), etch duration is 25 seconds, which corresponds to an etch depth of 7.9 μm.

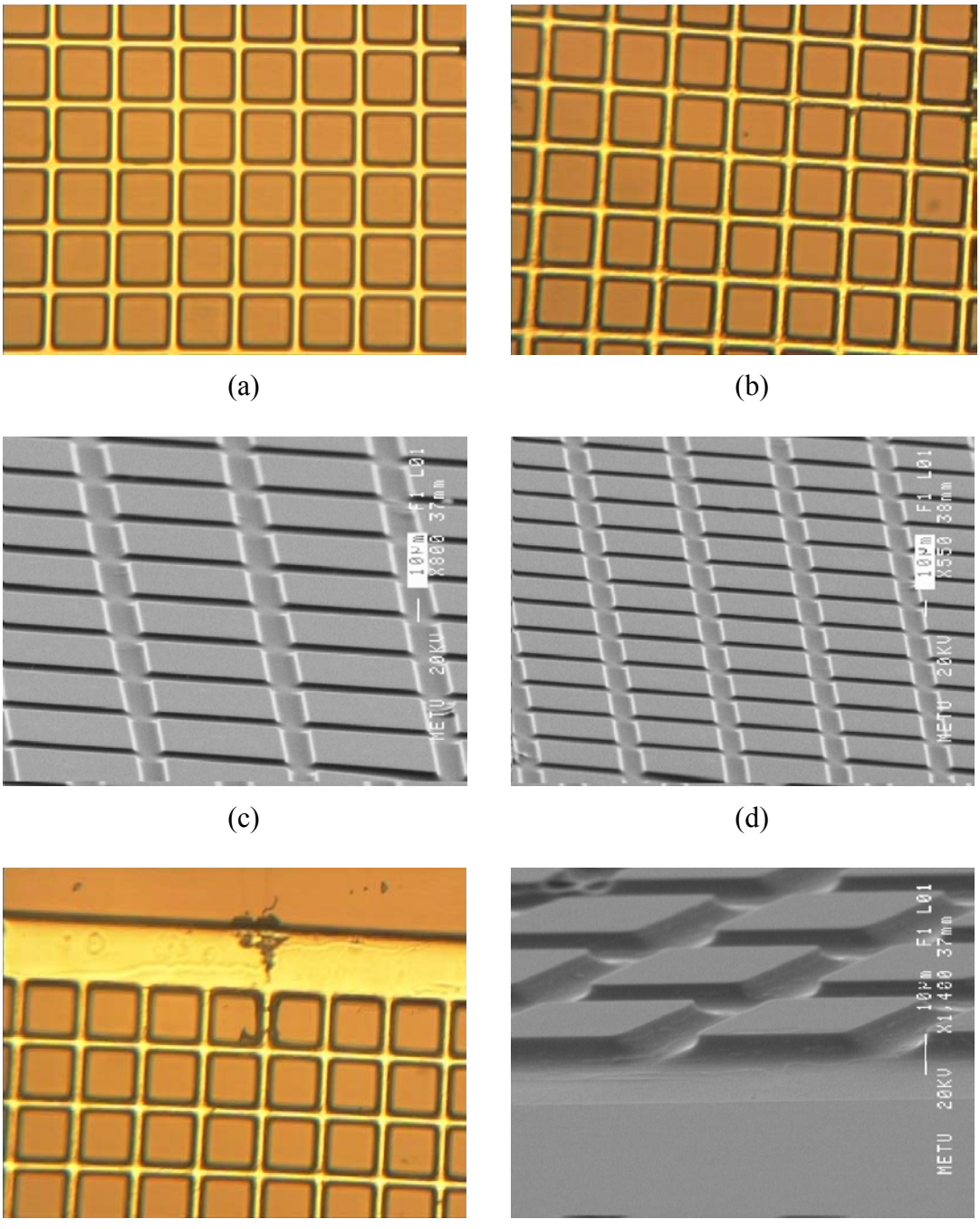

Figure 4.6: (a) etch duration is 10 seconds (optical microscope); (b) etch duration is 15 seconds (optical microscope); (c) and (d) both etch durations are 10 seconds (SEM); (e) and (f) etch durations are 25 seconds.

4.1.2 Ohmic Contact Study

Good ohmic contact formation is challenging especially for p on n $Hg_{1-x}Cd_xTe$ infrared detectors. Some of the issues related with ohmic contacts in photodiodes are contact resistance, contact surface recombination, contact 1/f noise, and long-term and thermal stability of the device.

The key parameter for determining the electrical properties of metal contacts is the Fermi level in the semiconductor at the semiconductor metal interface, which is designated as E_{fi}. For an n-type semiconductor, if E_{fi} lies in the conduction band, corresponding metal contact characteristic will be ohmic. Otherwise, metal contact characteristic will be rectifying due to Schottky barriers. On the other hand, for a p-type semiconductor, if E_{fi} lies in the valence band, corresponding metal contact characteristic will be ohmic. Otherwise, metal contact characteristic will be rectifying [41]. For $Hg_{1-x}Cd_xTe$ with $x<0.4$, ohmic contacts can easily be established on n-type material, however metal contacts tend to be rectifying on p-type material. For $x>0.4$, rectifying contact formation is expected for both n-type and p-type materials (due to formation of Schottky barriers) [12].

Metals can be grouped into four different classes with respect to the relative heat of formation of HgTe and the corresponding metal telluride [42]. This classification is as follows [42]:

- Ultrareactive
- Reactive
- Intermediate
- Unreactive

Ultrareactive group includes Ti, Sm, and Yb, and reactive group includes Al, In, and Cr [42]. Deposition of ultrareactive and reactive metals on $Hg_{1-x}Cd_xTe$ results in formation of metal tellurides, which are more stable than HgTe and causes loss

of Hg from the interfacial region. Hence, modification of $Hg_{1-x}Cd_xTe$ stoichiometry occurs in the interfacial region. On the other hand, deposition of unreactive metals such as Au or Sb, results in a stoichiometric interface with no loss of Hg [42]. The most popular contact metal for n-type $Hg_{1-x}Cd_xTe$ is In which is also used for n-type doping widely in MBE and LPE growths. Indium contacts show ohmic characteristic for x=0.30–0.68 [43]. Ohmic contacts to p-type $Hg_{1-x}Cd_xTe$ are more difficult since p-type $Hg_{1-x}Cd_xTe$ has a high work function, and a high work function metal is necessary for ohmic contact formation. Electroless Au and evaporated Au are used to produce ohmic contacts on p-type $Hg_{1-x}Cd_xTe$ [44, 45]. However, evaporated and electroless Au contacts tend to produce mechanically weak interfaces with $Hg_{1-x}Cd_xTe$ which result in high contact resistance, poor reproducibility, rectification at low temperatures [46]. Electroless Au contacts, formed by immersion of $Hg_{1-x}Cd_xTe$ sample into $AuCl_3$ solution, have a thin oxychloride layer at the Au/$Hg_{1-x}Cd_xTe$ interface and are very frail to lifting and peeling. On the other hand, metals reacting chemically with $Hg_{1-x}Cd_xTe$ displace Hg atoms and can result in type conversion and rectifying contacts. HgTe, which is a semimetal with a high work function, is a good candidate as a contact metal for p-type $Hg_{1-x}Cd_xTe$. HgTe sticks well to $Hg_{1-x}Cd_xTe$ and forms very stable contacts [33, 44, 45].

In this study, various metals and methods were investigated to form good ohmic contacts to p-type $Hg_{1-x}Cd_xTe$ as explained in the following sections.

4.1.2.1 Chromium (Cr) Contacts

Chromium (Cr) is used as a contact metal for p-type $Hg_{1-x}Cd_xTe$ [46]. $Hg_{1-x}Cd_xTe$ epilayer structure used in this study is the same as the one given in Figure 3.1 (a). Cr and Au were deposited on this $Hg_{1-x}Cd_xTe$ sample by thermal evaporation (Cr is in contact with $Hg_{1-x}Cd_xTe$, Au is deposited over Cr). Prior to metal deposition, a very short etching was applied with Br_2/HBr to regions where metal would be deposited. Metal contacts had dimensions of 250 μm x 250 μm. After the process was finished, I-V characteristics of p-to-p metal contacts were investigated in

liquid nitrogen (77 K). The contacts showed rectifying characteristic of two back to back connected diodes instead of a linear characteristic. After the characterization, this sample was annealed in an oven in atmospheric conditions first for 16 hours at 85ºC, then for 2 hours at 100ºC. In Figure 5.6 I-V characteristics of p-to-p contacts on $Hg_{1-x}Cd_xTe$ before and after annealing are given. Application of the adopted annealing process did not seem to alter the rectifying characteristic of p-to-p contacts.

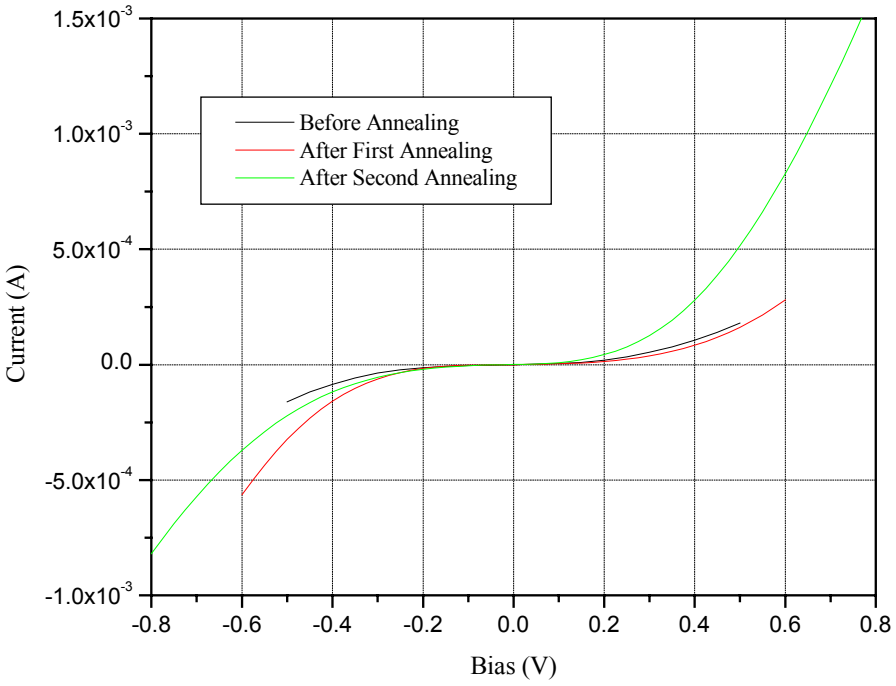

Figure 4.7: I-V characteristics of test sample with Cr/Au metal contacts before and after annealing processes.

4.1.2.2 Gold (Au) Contacts

Gold (Au) is frequently used for p-type $Hg_{1-x}Cd_xTe$ as a contact metal [47]. Au has a high work function and acts as a p-type dopant for $Hg_{1-x}Cd_xTe$. On the other hand, it diffuses into $Hg_{1-x}Cd_xTe$, and in the long term, it can cause photodiode instability. In this work, to investigate the potential of Au as an ohmic contact metal, p-to-p Au contacts were formed on p-type $Hg_{1-x}Cd_xTe$, and then

characterized in liquid nitrogen. I-V characterization results of the samples prepared according to Methods 1 and 2 described below are given in Figure 4.8.

Method 1

- $Hg_{1-x}Cd_xTe$ epilayer structure is the same as in Figure 3.1 (a)
- Metal contact lithography
- A short etching by HF/H_2O solution
- Plasma cleaning with 50 W O_2 plasma for 30 seconds [45]
- Deposition of Au by thermal evaporation

Method 2

- $Hg_{1-x}Cd_xTe$ epilayer structure is the same as in Figure 3.1 (a)
- Metal contact lithography
- A short etching by Br_2/HBr solution
- Deposition of a thin Au layer by thermal evaporation
- Immersion into $AuCl_3/H_2O$ solution [33, 45]

As shown in Figure 4.8, the results of the above study did not reveal good ohmic formation on p-type HgCdTe with Au.

4.1.2.3 Platinum (Pt) Contacts

Platinum is another high work function metal. However; Pt acts as an n-type dopant for $Hg_{1-x}Cd_xTe$ [48]. In order to investigate the potential of Pt as an ohmic contact metal, p-to-p Pt contacts were formed on p-type $Hg_{1-x}Cd_xTe$, and then characterized in liquid nitrogen. Process steps are given below. I-V characterization results are given in Figure 4.8. Pt did not seem to be a good choice for good ohmic contact formation on p-type HgCdTe.

- $Hg_{1-x}Cd_xTe$ epilayer structure is the same as in Figure 3.1 (a)
- Metal contact lithography

- A short etching by Br_2/HBr solution
- Plasma cleaning with 80 W O_2 plasma for 60 seconds
- Deposition of Pt and Au layer by thermal evaporation (Au is deposited over Pt)

4.1.2.4 Copper (Cu) Contacts

Copper (Cu) acts as a p-type dopant for $Hg_{1-x}Cd_xTe$, however it is also a fast diffuser in $Hg_{1-x}Cd_xTe$, which causes uncertainties in the stability of photodiodes in the long term [48]. In order to investigate the potential of Cu as an ohmic contact metal, p-to-p Cu contacts were formed on p-type $Hg_{1-x}Cd_xTe$, and then characterized in liquid nitrogen. Process steps are given below. I-V characterization results are given in Figure 4.8. Cu also failed to be a good ohmic contact metal for p-type HgCdTe.

- $Hg_{1-x}Cd_xTe$ epilayer structure is the same as in Figure 3.1 (a)
- Mesa etch lithography and mesa etch (Mesa dimensions are 300 μm x 300 μm)
- Metal contact lithography (Each mesa has two 100 μm x 100 μm contacts)
- A short etching by Br_2/HBr solution
- Plasma cleaning with 80 W O_2 plasma for 60 seconds
- Deposition of Cu and Au layer by thermal evaporation (Au is deposited over Cu)

4.1.2.5 HgTe Contacts

After all of the efforts toward making ohmic contacts on p type $Hg_{1-x}Cd_xTe$ with thermally evaporated various metals had failed, some of the samples having the epilayer structure of Figure 3.1 (a) were ex-situ HgTe deposited with an MOVPE system by Vigo Systems S.A. In the literature it is reported that it is possible to establish ohmic contacts on p-type $Hg_{1-x}Cd_xTe$ by HgTe deposition [33]. As explained in the following sections and as shown in Figure 4.8, nearly linear I-V

characteristics were obtained with HgTe deposited epilayers reflecting reasonably good ohmic contact formation.

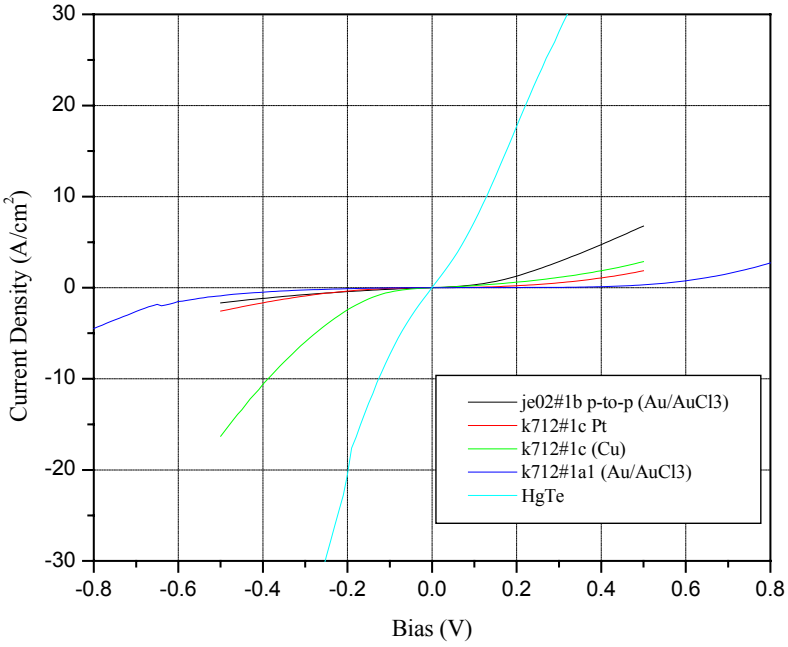

Figure 4.8: Comparison of current density versus bias voltage characteristics of various p-to-p $Hg_{1-x}Cd_xTe$ metal contacts.

4.2 128x128 $Hg_{1-x}Cd_xTe$ FPA Fabrication

After studying the most challenging steps of the p on n $Hg_{1-x}Cd_xTe$ FPA, the other steps of the FPA fabrication were optimized. Each fabrication step needs some precautions to be taken due to the nature of HgCdTe as a material difficult to process.

Some of the steps of the FPA fabrication are given in the following subsections.

4.2.1 Alignment Mark Process

- Photoresist (S1828) spin
- Photoresist Bake
- Expose to UV
- Develop with MF312 solution

- Etch with Br_2/HBr solution for 5 seconds
- Plasma Cleaning: 80 W O_2 plasma for 60 seconds
- Metal Deposition: Cr / Au by thermal evaporation,
- Lift-off

4.2.2 Mesa Etch Process

- Photoresist (S1828) spin
- Photoresist Bake
- Expose to UV
- Develop with MF312 solution for 50 seconds
- Etch: With Br_2/HBr solution until etch depth is equal to 4 μm

Figure 4.9 shows the photograph of the sample after mesa etching is completed.

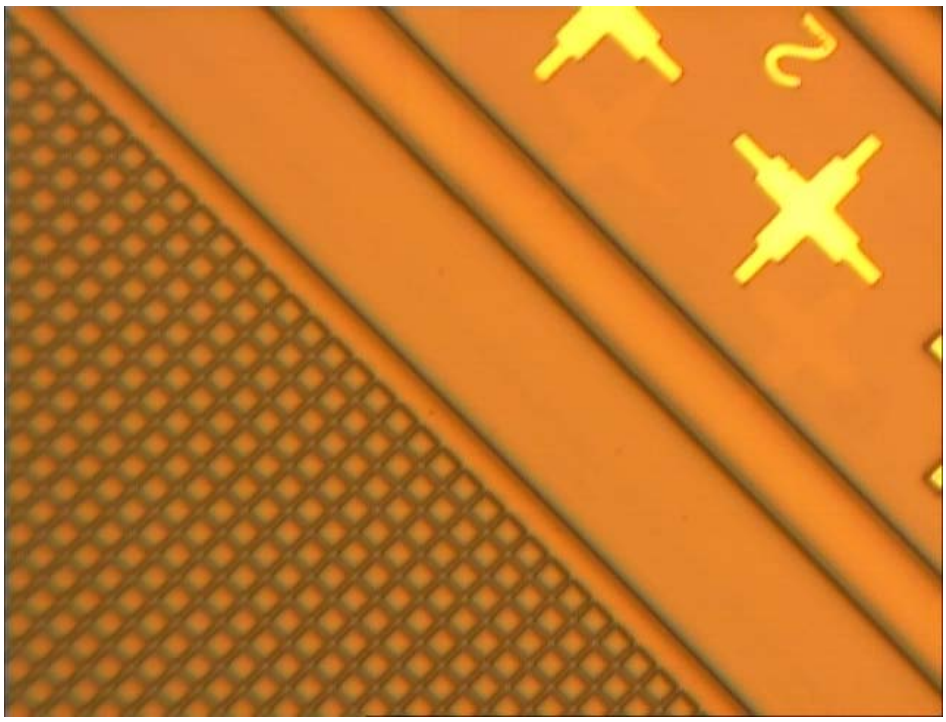

Figure 4.9: 128x128 $Hg_{1-x}Cd_xTe$ FPA after mesa etch process is finished.

4.2.3 Metal Contact Deposition Process

- Photoresist (S1828) spin
- Photoresist Bake
- Expose to UV
- Develop with MF312 solution for 30 seconds
- Etch with Br_2/HBr solution for 5 seconds
- Plasma Cleaning: 80 W O_2 plasma for 60 seconds
- Metal Deposition: Cr / Au by thermal evaporation
- Lift-off

Figure 4.10 shows the photograph of the sample after ohmic contact deposition is completed.

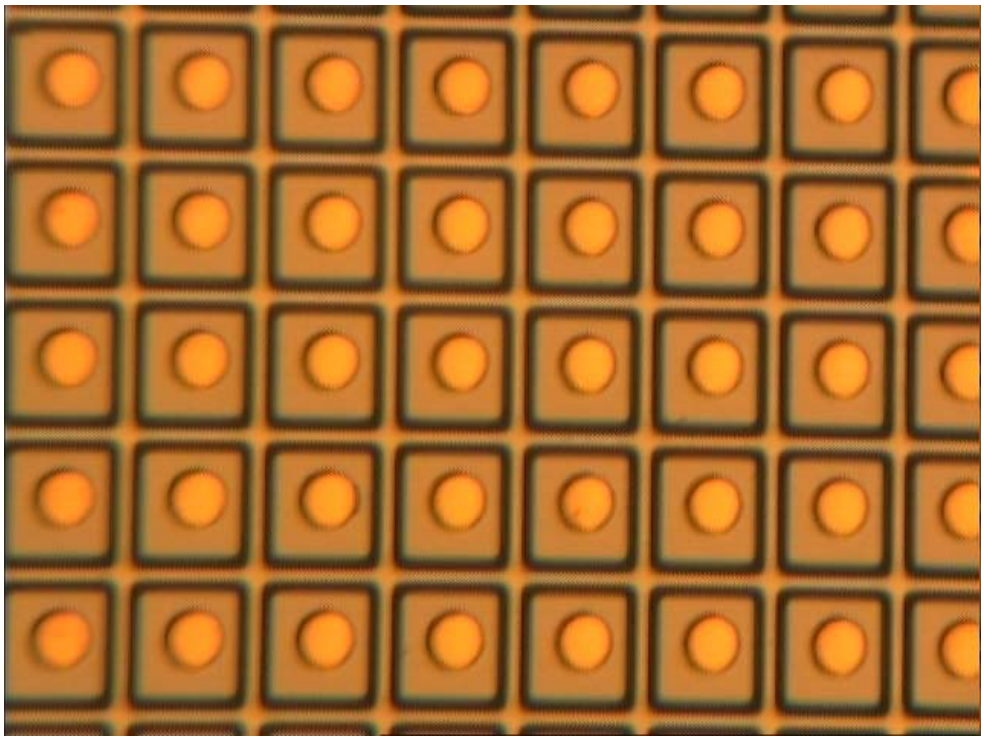

Figure 4.10: 128x128 $Hg_{1-x}Cd_xTe$ FPA after ohmic contact process is finished.

4.2.4 Pasivation Material Deposition and Etch Process

- Plasma Cleaning: 80 W O_2 plasma for 60 seconds
- CdTe Deposition by RF sputtering
- Photoresist (S1828) spin
- Photoresist Bake
- Expose to UV
- Develop: With MF312 solution
- Etch passivation material with Br_2/HBr solution

4.2.5 Under Bump Metal (UBM) Deposition Process

- Photoresist (S1828) spin
- Photoresist Bake
- Expose to UV
- Develop with MF312 solution
- Plasma Cleaning: 80 W O_2 plasma for 45 seconds
- UBM Deposition
- Lift-off

4.2.6 Indium (In) Electroplating Process

- Thick photoresist spin
- Photoresist Bake
- Expose to UV
- Develop with KOH solution
- Plasma Cleaning: 150 W O_2 plasma for 2 minutes
- Indium electroplating

Figure 5.11 shows a photograph of the FPA after In electroplating.

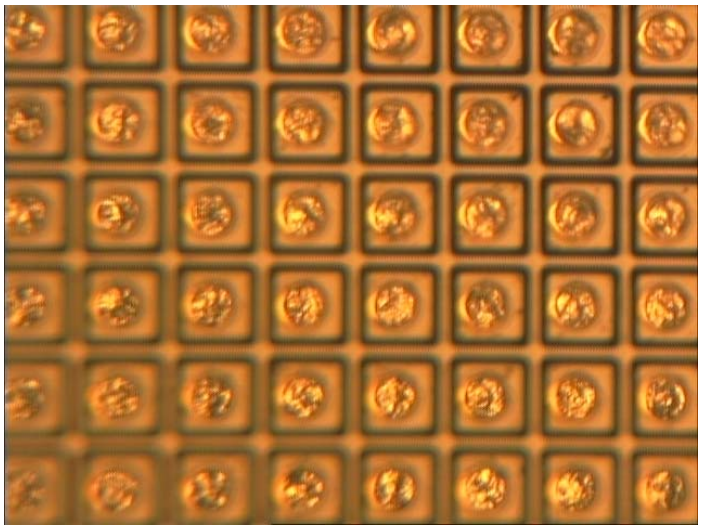

Figure 4.11: a photograph of the FPA after In electro-plating.

4.2.7 ROIC Post Processing

Since HgCdTe epilayers cannot withstand temperatures above 80ºC, cold compression during flip-chip bonding (hybridization) is necessary. This can be possible if In bumps are formed on both the detector array and the ROIC. Therefore, In electroplating was also performed on the ROIC before the hybrid integration.

In Figure 4.12, a photograph of the ROIC taken by an optical microscope after the UBM deposition and In-electroplating processes are completed.

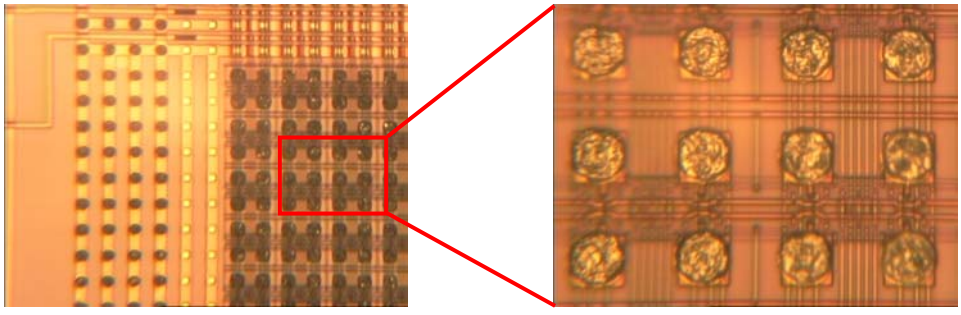

(a) (b)

Figure 4.12: ROIC after In electroplating

4.2.8 Flip-Chip Bonding of FPA and ROIC

After the processing of the detector array and the ROIC were completed, they were hybridized using RD Automation M8–AN flip-chip aligner bonder. During the bonding neither the FPA nor the ROIC were heated. After the ROIC and the FPA were integrated, the gap between them (< 10 μm) was completely filled with a proper underfill epoxy, and the epoxy was cured.

This chapter presented the work on the fabrication steps of 128x128 HgCdTe FPA. The FPA performance and the pixel characteristics will be given in the next chapter.

CHAPTER 5

FOCAL PLANE ARRAY AND PIXEL CHARACTERISTICS

This chapter presents the characteristics of the photodiodes fabricated with the epilayer structures shown in Figure 3.1 (b), as well as the performance of 128x128 $Hg_{1-x}Cd_xTe$ FPAs fabricated with the process described in the previous chapter. I will first present and discuss the characteristics of the FPA pixel sized photodiodes before presenting the results obtained with the 128x128 FPAs.

5.1 Electrical and Optical Measurement Set Ups

The electrical characteristics of the $Hg_{1-x}Cd_xTe$ photodiodes were evaluated with Keithley 238 High Current Source Measure Unit under computer control. The block diagram of the electrical measurement set up is shown in Figure 5.1 [49].

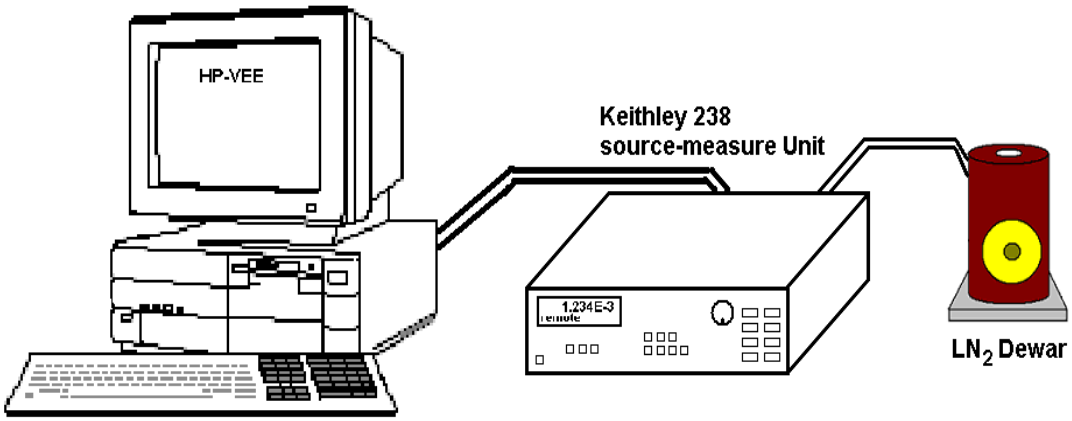

Figure 5.1: Block diagram of the electrical measurement set up [49].

The noise characteristics of photodiodes were measured by using Agilent 35670A Dynamic Signal Anlayzer. Detectors were cooled down to 77 K in a liquid nitrogen dewar. Stanford Research Systems SR570 Low Noise Current Preamplifier was used to bias the photodiodes. A low noise preamplifier was used to amplify noise signals. Batteries were used as power supply for the amplifier. In Figure 5.2 the noise measurement setup is illustrated [49].

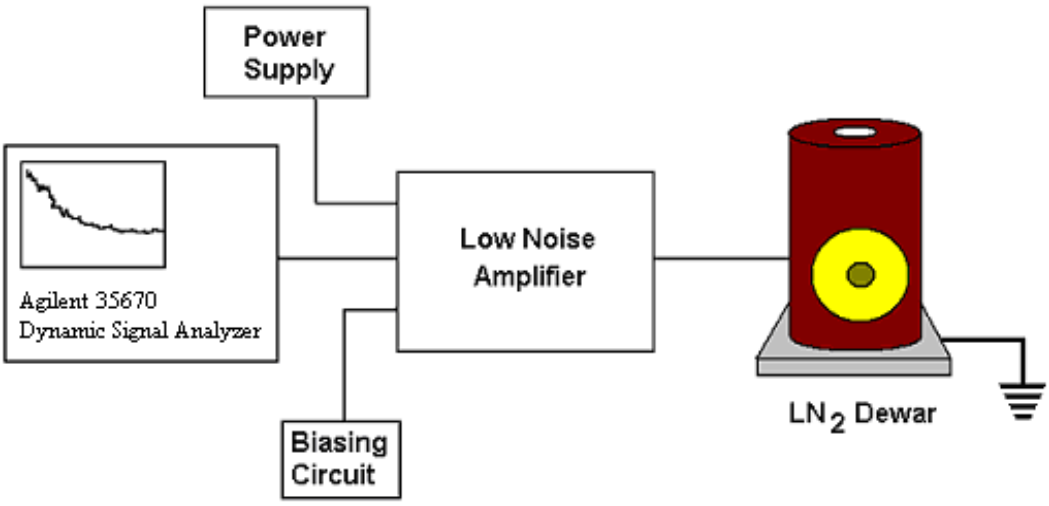

Figure 5.2: Noise measurement setup [49].

The optical characteristics of the photodiodes were measured using a black body source/chopper assembly, lock-in amplifier, preamplifier and a Fourier transform interferometer (FTIR) system, all under computer control. Block diagrams of the

set-ups utilized in optical measurements are shown in Figure 5.3 [49]. For the responsivity and detectivity measurement, the low noise transimpedance preamplifier amplifies the blackbody radiation modulated by the chopper, and the detector signal is fed into a lock-in amplifier, which is locked to the chopper frequency. Oriel MIR-8000 FTIR system was utilized for measuring the spectral response of the photodiodes. The detector signal was referenced to that of a pyroelectric detector with a wide-band spectral response.

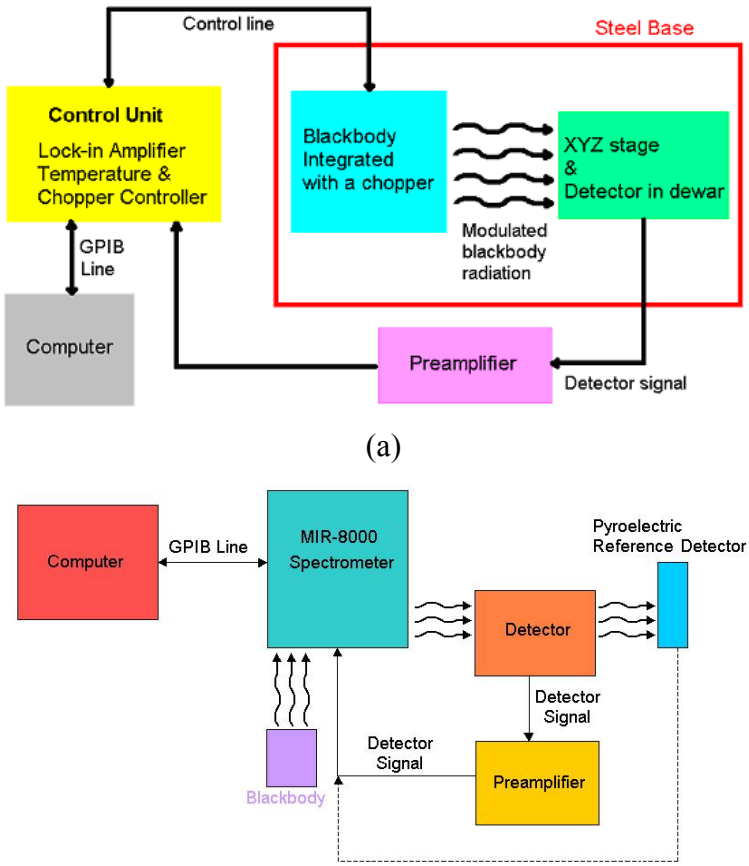

Figure 5.3: Block diagram of the optical measurement set up [49].

5.2 $Hg_{1-x}Cd_xTe$ Photodiode Characteristics

The photodiodes fabricated with the epilayer structures shown in Figure 3.1(b) were subjected to electrical and optical characterization, and the 77 K dark

currents of the photodiodes were subjected to modeling in order to reveal the performance limiting mechanisms.

5.2.1 Electrical Characteristics

A test process is performed to investigate the electrical and optical characteristics of the $Hg_{1-x}Cd_xTe$ diodes. The test process consists of the following steps

- Mesa etch
- Metal contact deposition
- Passivation
- Fan-out metallization

Mesas were etched down to the n-type $Hg_{1-x}Cd_xTe$ layer and the isolation of mesas is performed. Ohmic contacts were formed on the HgTe layer by Cr and Au deposition by thermal evaporation (See Figure 3.1 (b)). After the ohmic contact formation, mesas were passivated by CdTe, which was deposited by RF sputtering. Finally, fan-out lines and metal pads were formed by Cr and Au deposition through thermal evaporation.

In Figure 5.4 I-V characteristic of a 33x33 μm^2 $Hg_{1-x}Cd_xTe$ (x=0.2196) diode is given. I-V measurement is taken at 77 K, and the diode is under zero illumination in order to avoid photocurrent generation. Diode has an R_0A product of 1.1 Ω-cm^2.

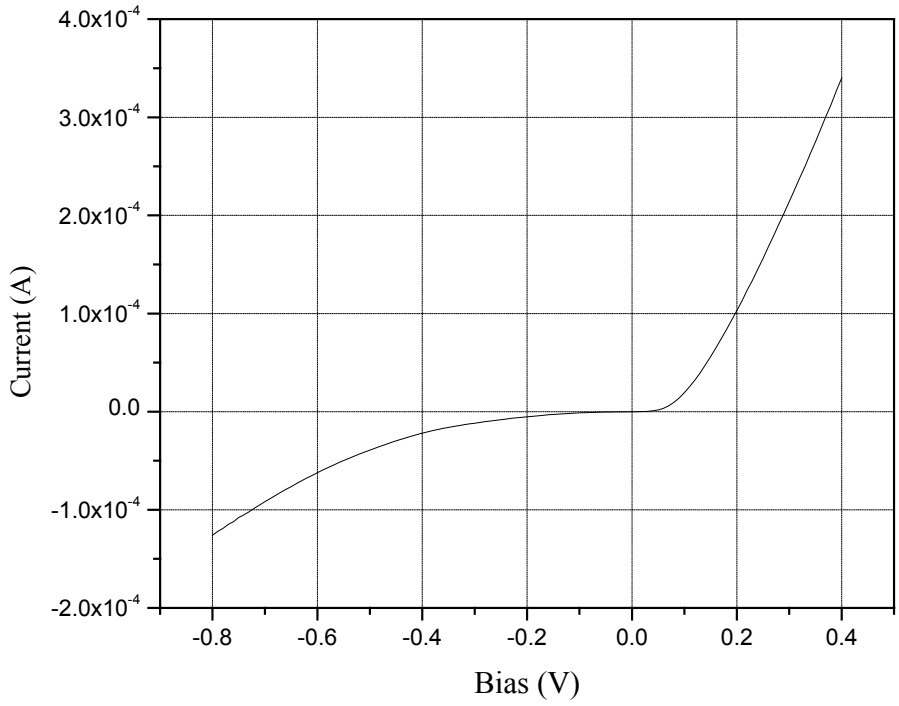

Figure 5.4: I-V characteristics of a 33x33 μm^2 $Hg_{1-x}Cd_xTe$ (x=0.2196) diode at 77 K under no illumination.

5.2.2 Optical Characteristics

Spectral responsivity versus wavelength characteristics of the 33x33 μm^2 $Hg_{1-x}Cd_xTe$ (x=0.2196) diode at 77 K are obtained by using the optical setup given in Figure 5.3 (b). The 50% cut-off wavelength of this material is 10.92 μm, which is in correspondence with the experimental cut-off wavelength as shown in Figure 5.5.

Detectivity and responsivity values of the same diode are measured by using the optical setup given in Figure 5.3 (a). D^*_{peak} value is measured as $3.2x10^{10}$ cm√Hz/W for the chopper frequency of 725 Hz. The measured peak responsivity is equal to 6.94 A/W.

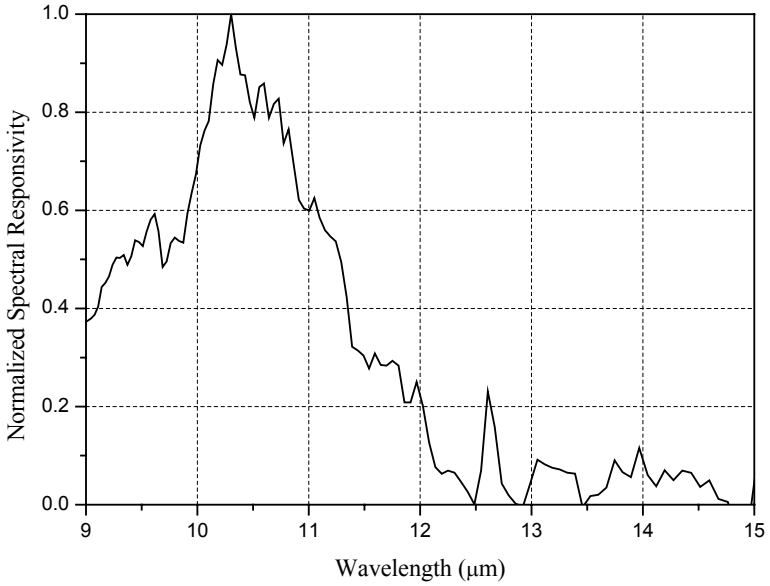

Figure 5.5: Normalized spectral responsivity versus wavelength obtained by FTIR measurement.

5.2.3 Dark Current Modeling

Dark current mechanisms in a p-n junction diode may originate from various sources, which may be related with the surface or bulk material. Determining the dominant dark current mechanisms is indispensable for enhancing the performance of the photodiodes by improving the material quality, redesigning the diode and the epilayer structure, or by improving the processing conditions. In order to identify the dominant dark current components, we have fit the sum of the presumably important dark current expressions to the experimental data over a sufficiently large bias range. The presumably important dark current mechanisms for $Hg_{1-x}Cd_xTe$ photodiodes of this study are diffusion, generation-recombination, trap assisted and band to band tunneling, and ohmic leakage due to possible electrically active dislocations in the material. The following sections briefly discuss these mechanisms before presenting the results of dark current modeling.

5.2.3.1 Diffusion current

Thermally generated minority carriers in p- and n-type regions diffuse to the other side of the junction and generate the diffusion current. Therefore, it is the fundamental current mechanism in a p-n junction. This mechanism occurs in the bulk region of the diode. Diffusion current density is given as [5]

$$J_{DIFF} = J_S\left[\exp\left(\frac{qV}{kT}\right)-1\right] \tag{5.1}$$

where V is the applied bias, k is the Boltzmann constant, T is the temperature, and J_s is the saturation current density given by [5]

$$J_S = q\left[\frac{D_n n_p}{L_n}+\frac{D_p p_n}{L_p}\right] \tag{5.2}$$

where D_n and D_p are electron and hole diffusion constants in cm^2/sec, n_p and p_n are electron and hole minority carrier concentrations in cm^{-3}, and L_n adn L_p are diffusion lengths in cm for electrons and holes in p-type and n-type regions, respectively.

5.2.3.2 Generation-Recombination Current

At low temperatures space charge region generation recombination current could be more dominant than the diffusion current. The generation rate in the depletion region can be very much greater than the generation rate in the bulk of the semiconductor even though the width of space charge region is much less than the diffusion length of minority carries [4].

In narrow gap semiconductors such as $Hg_{1-x}Cd_xTe$, there exist three fundamental generation-recombination mechanisms, which are Shockley-Read (S-R), radiative, and Auger. S-R mechanism is not a fundamental mechanism since it is

the direct result of S-R centers existing in the energy band gap due to native defects and foreign impurities in the semiconductor. Reduction of S-R mechanism is possible with the growth of purer and higher quality semiconductors [5].

Radiative process is the emission of a photon as a result of recombination of an electron and a hole. The radiative process depends on the energy band structure of the semiconductor and it is an intrinsic mechanism [5].

Auger mechanism is also an intrinsic process like the radiative process. Auger process is an important mechanism for the performance of narrow gap semiconductor infrared photon detectors. In the Auger mechanism a conduction band electron and a valence band hole recombines and a photon is generated. This photon interacts with another conduction band electron and excites it to a higher energy level in the conduction band. Afterwards, this excited electron interacts with crystal lattice and returns its initial state with an emission of a phonon [5]. Similar to radiative process, Auger process cannot be eliminated. This mechanism is an important recombination mechanism for n-type and p-type $Hg_{1-x}Cd_xTe$ diodes [4].

Generation-recombination current density is defined as [5]

$$J_{G-R} = \left(\frac{n_i W_o kT}{V_{bi} (\tau_e \tau_h)^{1/2}} + \frac{P s_o n_i W_o kt}{A V_{bi}} \right) \left(\frac{2 \sinh\left(\frac{qV}{2kT} \right)}{\left(\frac{V_{bi} - V}{V_{bi}} \right)^{1/2}} \right) f(b) \qquad (5.3)$$

where τ_e and τ_h are the carrier lifetimes of electrons and holes respectively, V is the applied bias, W_o is the zero bias depletion region width, s_o is the surface recombination velocity, V_{bi} is the built-in potential, and P and A are the perimeter and the area of the diode, respectively. $f(b)$ is defined as follows

$$f(b) = \int_0^\infty \frac{du}{u^2 + 2bu + 1} \tag{5.4}$$

where

$$b = \exp\left(-\frac{qV}{2kT}\right)\cosh\left(\frac{E_t - E_i}{kT} + \frac{1}{2}\ln\left(\frac{\tau_e}{\tau_h}\right)\right) \tag{5.5}$$

with E_i and E_t intrinsic and trapping energy levels, respectively [5] .

5.2.3.3 Tunneling Current

Tunneling current is the result of tunneling of electrons through the junction. If tunneling occurs directly from the valence band to the conduction band it is called as band-to-band tunneling (BTB) mechanism. If tunneling occurs from the valence band to the conduction band with the assistance of trap states located in the energy band gap, then it is called as trap assisted tunneling (TAT).

BTB is an important dark current mechanism for narrow gap semiconductors at high reverse bias voltages. BTB current density expression used in this dark current modeling study is as follows [50]

$$J_{BTB} = 10^{-2} N_A^{1/2} V_t^{3/2} \exp\left[-\frac{3\times 10^{10} E_g^2}{(N_A V_t)^{1/2}}\right]. \tag{5.6}$$

TAT mechanism is due to tunneling of minority carriers from occupied trap states located either in the depletion region or in the quasi-neural region very close to the depletion edge [50]. The expression for differential resistance due to TAT mechanism is [51]

$$R_{TAT} = \frac{2}{qA_j Bc}\exp\left(\frac{c}{(V_b - V)^{1/2}}\right)(V_b - V)^{3/2} \tag{5.7}$$

where V_b is the built-in potential, V is the bias voltage, A_j is the diode area, B is a constant, and c is related with the energy levels of traps (E_t).

5.2.3.4 Ohmic Leakage Current

Ohmic leakage mechanism exhibits a shunt-like behavior in junction performance. It is a result of surface or bulk leakage currents. Ohmic leakage current can be expressed as [51]

$$I_S = \frac{V}{R_S} \tag{5.8}$$

where V is the applied voltage across the junction and R_S is the diode shunt resistance.

5.2.3.5 Dark Current Analysis

In order to obtain the dominant dark current mechanisms under various bias voltages at 77 K for the $Hg_{1-x}Cd_xTe$ photodiode whose I-V characteristics is given in Figure 5.4, a current model including diffusion, generation-recombination, band-to-band tunneling, trap assisted tunneling, and ohmic leakage mechanisms was used. The differential resistance expressions used in this dark current modeling study are given below [5, 50, 51]

$$R_{DIFF} = C_{DIFF} \exp\left(-\frac{qV}{kT}\right) \tag{5.9}$$

$$C_{DIFF} = \frac{kT}{qAJ_S} \tag{5.10}$$

$$(R_{G-R})^{-1} = \frac{1}{C_{G-R}} \frac{\partial f(V,T)}{\partial V} \tag{5.11}$$

$$f(V,T) = \left(\frac{2\sinh\left(\frac{qV}{kT}\right)}{\left(\frac{V_b - V}{V_b}\right)^{1/2}} \right) f(b) \tag{5.12}$$

$$\frac{1}{C_{G-R}} = A\left(\frac{n_i w_0 kT}{V_b \tau_0} + \frac{Ps_0 n_i w_0 kT}{AV_b} \right) \tag{5.13}$$

$$R_{TAT} = \frac{C_{TAT1}}{C_{TAT2}} \exp\left(\frac{C_{TAT2}}{(V_b - V)^{1/2}} \right) (V_b - V)^{3/2} \tag{5.14}$$

$$C_{TAT1} = \frac{2}{qA_j B} \tag{5.15}$$

$$C_{TAT2} = c \tag{5.16}$$

$$(R_{BTB})^{-1} = C_{BTB1}\left[-\frac{3}{2}(V_b - V)^{1/2} - \frac{C_{BTB2}}{2} \right] \exp\left(- C_{BTB2}(V_b - V)^{-1/2} \right) \tag{5.17}$$

$$C_{BTB1} = 10^{-2} A N_A^{-1/2} \tag{5.18}$$

$$C_{BTB2} = \frac{3 \times 10^{10} E_g^2}{N_A^{1/2}} \tag{5.19}$$

Equations (5.9–5.19) are derived directly by using the expressions given in the previous section. In these equations, C_{DIFF}, $C_{G\text{-}R}$, C_{TAT1}, C_{TAT2}, C_{BTB1}, and C_{BTB2} are the bias independent parameters whose values depend on temperature and

semiconductor properties. These parameters were varied to fit Equations (5.9–5.19) to the experimental data. The material parameters for this epilayer structure (See Figure 3.1 (b)) used for the fitting purposes are given in Table 5.1.

Table 5.1: Material parameters for $Hg_{1-x}Cd_xTe$ (x=0.2196) structure at 77 K used in dark current modeling study

N_A (cm^{-3})	N_D (cm^{-3})	E_g (eV)	n_i (cm^{-3})	V_b (V)	w_0 (cm)	ε_s (F/m)
$2x10^{17}$	$2x10^{15}$	0.1136	$1.1x10^{13}$	$9.97x10^{-2}$	$3.108x10^{-7}$	$1.54x10^{-10}$

In Table 5.1, N_A is the acceptor concentration of the p-type $Hg_{1-x}Cd_xTe$ layer, N_D is the donor concentration of the n-type $Hg_{1-x}Cd_xTe$ layer, E_g is the energy band gap, n_i is the intrinsic carrier concentration, V_b is the built in potential, w_0 is the width of the depletion region, and ε_s is the static dielectric constant.

The differential resistance of the detector can be considered as the parallel combination of all the resistance components due to the dark current mechanisms. Hence the differential resistance can be expressed as follows

$$\frac{1}{R} = \frac{1}{R_{DIFF}} + \frac{1}{R_{TAT}} + \frac{1}{R_{G-R}} + \frac{1}{R_S} + \frac{1}{R_{BTB}} \tag{5.20}$$

where R_S is the shunt resistance due to ohmic leakage, R_{DIFF} is the resistance representing the diffusion mechanism of dark current, R_{G-R} represents the differential resistance arising from the generation-recombination mechanism, R_{TAT} is the differential resistance modeling the trap assisted tunneling mechanism of dark current, and finally R_{BTB} models the band-to-band tunneling mechanism of dark current. Figure 5.6 shows the differential resistance versus bias voltage characteristic of the 33x33 μm^2 $Hg_{1-x}Cd_xTe$ diode at 77 K and the results of the dark current modeling study.

Figure 5.6 reveals that ohmic leakage and diffusion mechanisms do not have significant contributions to dark current in the investigated bias region at 77 K. At higher reverse bias voltages, BTB is the dominant dark current mechanism as expected [52]. For small reverse bias voltages dark current is mostly produced by TAT mechanism. Under small forward bias, generation-recombination is the dominant mechanism for this detector. The modeling results for the reverse bias voltages of this study match with some reported studies in the literature [52].

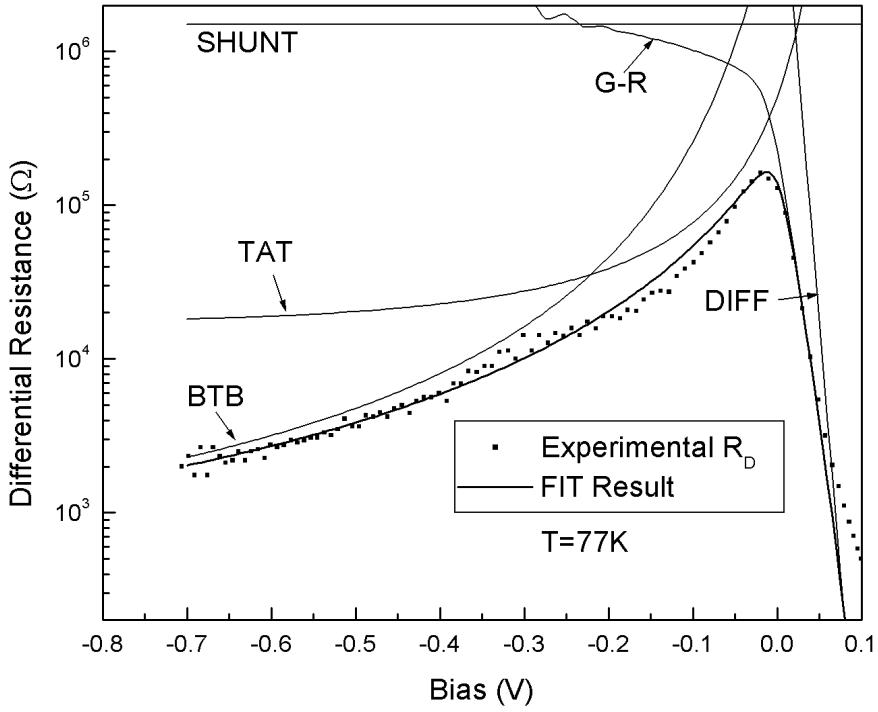

Figure 5.6: The measured and calculated differential resistance of $Hg_{1-x}Cd_xTe$ (x=0.2196) diode at 77 K.

5.2.4 Detector Noise Analysis

Noise measurements for the $Hg_{1-x}Cd_xTe$ photodiode are performed by using the setup given in Figure 5.2 in the 0–6.4 kHz range. The equivalent circuit of the noise measurement setup, which used in order to extract the detector noise from the measured noise is shown in Figure 5.7.

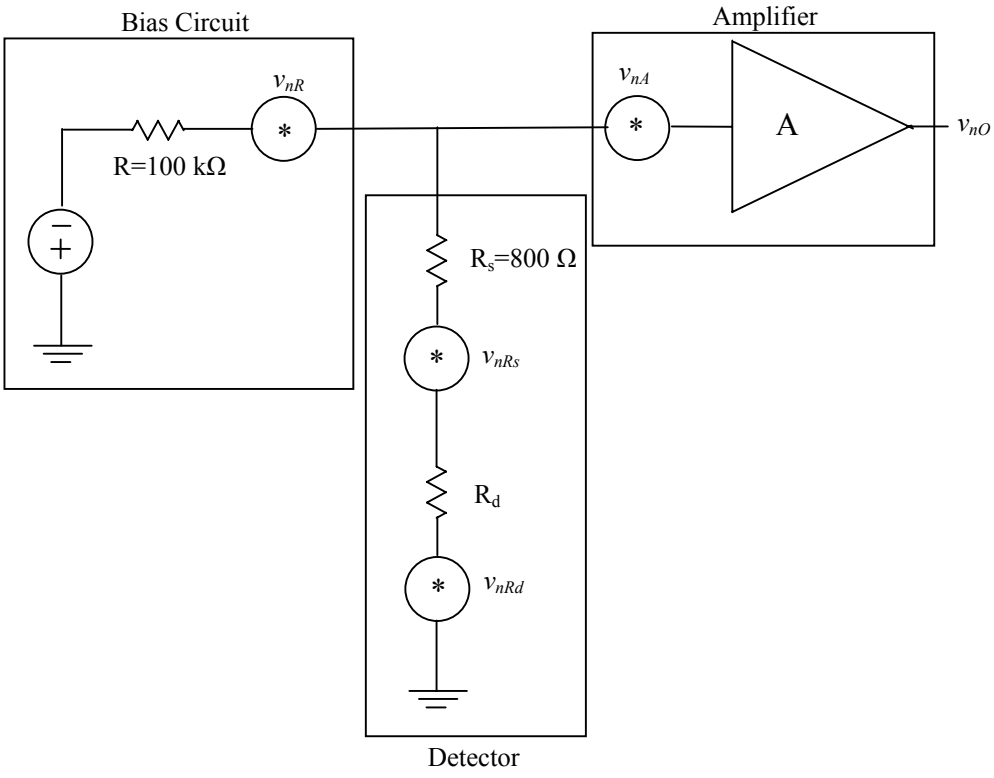

Figure 5.7: Equivalent circuit of the noise measurement setup.

The other noise components were extracted from the measured voltage noise spectral density, namely v_{nO} by using the following expression

$$\left(\frac{v_{nO}}{A}\right)^2 = (v_{nA})^2 + \left(\frac{v_{nR}(R_d + R_s)}{R + R_d + R_s}\right)^2 + \left(\frac{v_{nRs}R}{R + R_d + R_s}\right)^2 + \left(\frac{v_{nRd}R}{R + R_d + R_s}\right)^2 . \qquad (5.21)$$

In Equation (5.21), A represents the amplifier gain which is given as a function of frequency in Figure 5.8, v_{nA} is the input referred amplifier voltage noise spectral density, v_{nR} is the thermal noise of the resistor of the bias circuit, v_{nRs} is the thermal noise due to the serial resistance of the detector, v_{nRd} is the detector voltage noise spectral density, R is bias circuit resistance, R_s is the detector serial resistance, and finally R_d is the dynamic resistance of the detector at the corresponding bias voltage. Thermal noise of the resistors were calculated with the help of the following expression [53]

$$v_{nR} = \sqrt{4kTR} \tag{5.22}$$

where k is the Boltzmann's constant, T is temperature, and R is resistance.

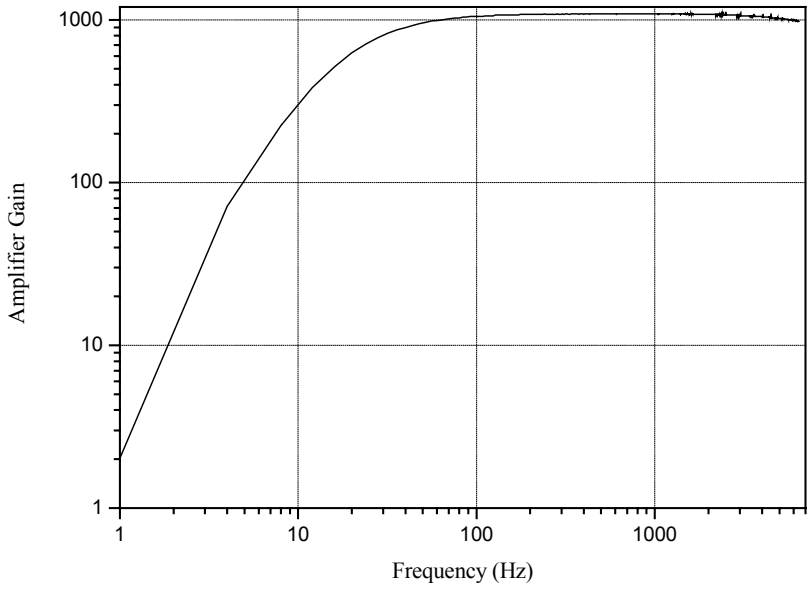

Figure 5.8: Amplifier gain as a function of frequency.

After v_{nRd} was determined by using Equation (5.21), corresponding noise current spectral density i_{nRd} was calculated with the following expression

$$i_{nRd} = \frac{v_{nRd}}{R_d}. \tag{5.23}$$

Voltage noise spectral density was measured for the following detector voltage biases: -5 mV, -10 mV, -20 mV, -40 mV, -60 mV, -80 mV, -100 mV, -125 mV, and -150 mV. In Figure 5.9 the corresponding detector current noise spectral density plots as a function of frequency are given.

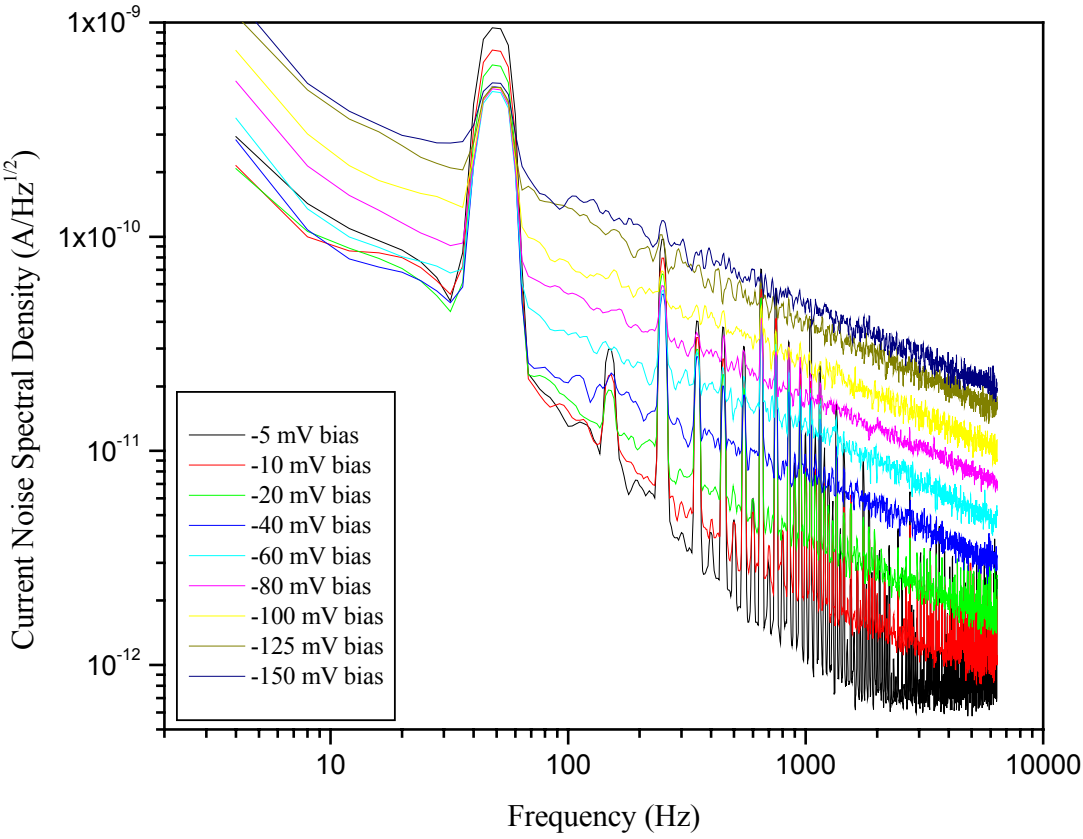

Figure 5.9: Detector current noise spectral density as a function of frequency at detector bias voltages between -5 mV to -150 mV.

By using the current noise spectrum density results, 1/f noise at 1 Hz is determined for all bias voltages that are under consideration. At 77 K, 1/f noise is expected to be dominated by the trap assisted tunneling dark current process [54]. In Figure 5.10 1/f noise current at 1 Hz with respect to the detector trap assisted tunneling current plot is given. As the curve fitting shows, 1/f noise current at 77 Kcan be expressed as follows

$$i_n = \alpha_{TAT}(I_{TAT})^{\beta} \tag{5.24}$$

with α_{TAT} = 7x10^{-5}, and β = 0.65. These α_{TAT} and β values are not far away from those of obtained by Nemirovsky and Unikovsky (α_{TAT} = 1x10^{-6}, and β = 0.5) for $Hg_{1-x}Cd_xTe$ [54].

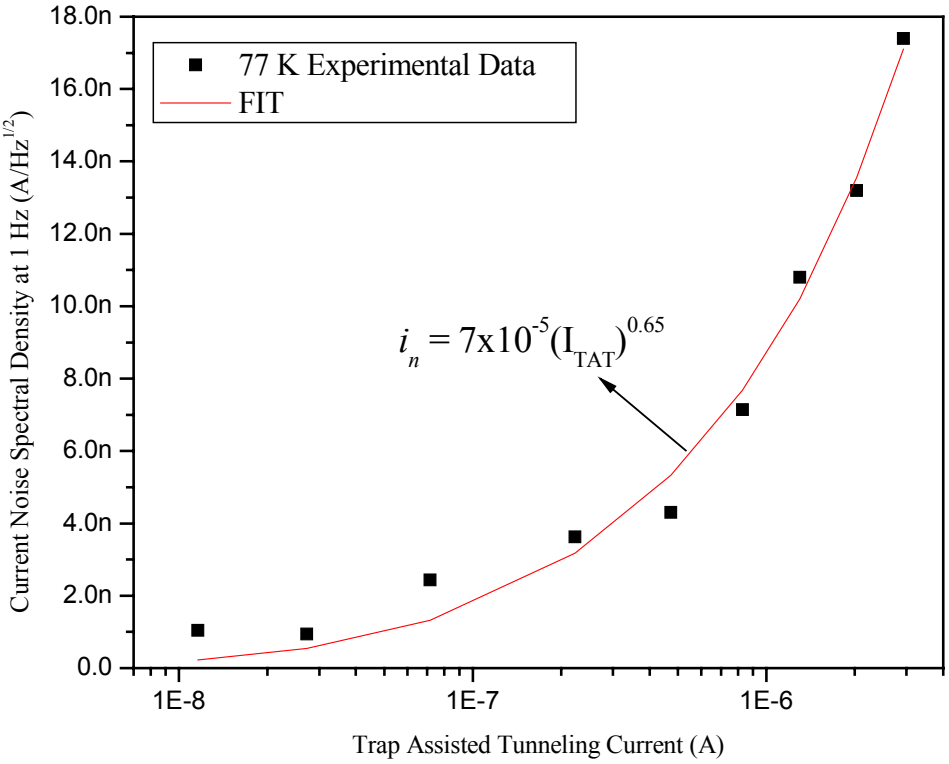

Figure 5.10: 1/f noise of detector as a function of detector trap assisted tunneling current.

5.3 Real Time Thermal Imaging with 128 x 128 $Hg_{1-x}Cd_xTe$ FPAs

128x128 $Hg_{1-x}Cd_xTe$ FPA-ROIC hybrid was placed in an 84-pin leadless chip carrier (LCC) package. This LLC package was then installed into Indigo Systems' ISC9801 Standard 128 evaluation camera, which is shown in Figure 5.11. Real time images were taken with two FPAs. One of the FPAs has a p-on-n double layer heterojunction structure (See Figure 3.1 (b)) with CdTe mole fraction of 0.2136, which correspond to a cut-off wavelength of 11.94 µm. The other FPA has a p-on-n homojunction structure (See Figure 3.1 (c)) with CdTe mole fraction of 0.2245, which corresponds to a cut-off wavelength of 10.21 µm. It should be

noted that FPAs fabricated and investigated in this thesis were not optimized in terms of anti reflection coating deposition, and substrate lapping and polishing.

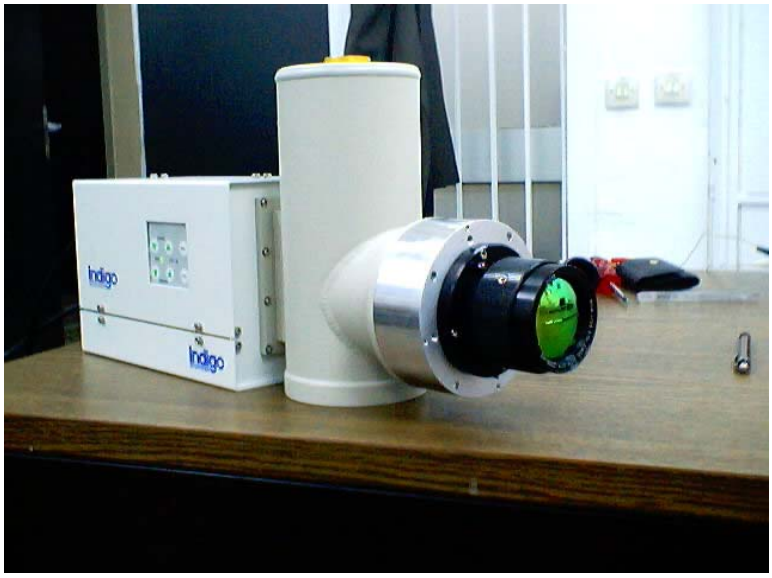

Figure 5.11: Indigo Systems' ISC9801 Standard 128 evaluation camera [49].

In Figure 5.12, two snapshots from the real time movies of a solder gun at 400ºC were taken by the heterojunction $Hg_{1-x}Cd_xTe$ FPA with x=0.2136 are given. Due to the low R_0A product (1.1 Ω-cm^2) of the photodiodes and large nonuniformity (resulting from high cut-off wavelength) only hot objects can be imaged with the fabricated 128x128 $Hg_{1-x}Cd_xTe$ FPA. As shown in Figure 5.6, the R_0A product of the pixels can be improved by nearly an order of magnitude if the trap assisted tunneling current can be decreased by improving the growth condition of the $Hg_{1-x}Cd_xTe$ epitaxial layers. However, improvement of the FPA uniformity still presents a challenging problem. The FPA fabricated with the homojunction structure (Figure 3.1 (c)) yielded worse results due to the lower R_0A product (0.008 Ω-cm^2). While nearly 100% pixel yield was achieved in the fabrication process, a considerable portion of the pixels were defected possibly due to the defects in the material.

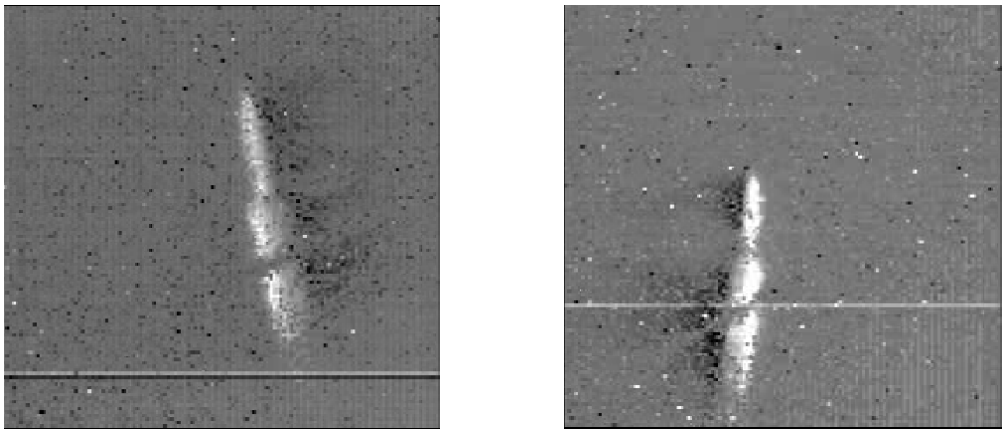

(a) (b)

Figure 5.12: Snapshots from real time movies taken by 128 x 128 heterojunction FPA.

CHAPTER 6

CONCLUSIONS

This thesis reports the fabrication and characterization of long wavelength infrared heterojunction $Hg_{1-x}Cd_xTe$ photodiodes and 128x128 focal plane arrays grown on lattice matched $Cd_{1-y}Zn_yTe$ substrates by MOVPE. HgCdTe is a material difficult to process for device fabrication due to some unique properties of the alloy. In this thesis work, the fabrication and integration steps of long wavelength HgCdTe FPAs were developed, and 128x128 $Hg_{1-x}Cd_xTe$ FPAs were successfully fabricated and tested. In order to test the pixel characteristics of the FPAs, small test detectors having the same structure and dimensions with the FPA pixels were fabricated and characterized.

Electrical and optical characterization results of 33x33 μm^2 $Hg_{1-x}Cd_xTe$ (x=0.2196) heterojunction photodiodes were carried out at 77 K. The investigated photodiode yielded an R_0A value of 1.1 Ωcm^2 at 77 K. The dark current modeling study indicated that band to band tunneling, trap assisted tunneling, and generation-recombination mechanisms dominate the dark current under high reverse bias, small reverse bias, and low forward bias, respectively. Spectral responsivity plot is found to be in correspondence with the theoretical 50% cut-off wavelength value (10.9 μm). The peak 80 K detectivity of the investigated photodiode is $3.2x10^{10}$ cm√Hz/W, and the responsivity of the detector is 6.94 A/W corresponding to a quantum efficiency of 78%.

After the development of the fabrication procedures, 128x128 $Hg_{1-x}Cd_xTe$ focal plane arrays were fabricated, and hybridized with read-out integrated circuits. More work needs to be done for the optimization of the material characteristics and the diode structure in order to decrease the dark current and increase the RoA product of the detectors. Especially, the trap assisted tunneling current must be decreased to improve the R_0A product of the diodes under small reverse bias. Due to the low R_0A product and high nonuniformity arising from high cut-off wavelength, only hot objects could be imaged with the fabricated FPAs.

REFERENCES

[1] A. Rogalski, "Infrared Detectors: an overview", *Infrared Physics & Technology*, vol. 43, pp. 187-210, 2002.

[2] G.Gaussorgues, S. Chomet, *Infrared Thermography*, Chapman&Hall, 1994.

[3] A.Rogalski, K. Chrzanowski, "Infrared devices and techniques", *Opto-Electronics Review*, vol. 10(2), pp. 111-136, 2002.

[4] Gerald C. Holst, *Testing and Evaluation of Infrared Imaging Systems*, JCD Publishing and SPIE Optical Engineering Press, 1998.

[5] A. Rogalski, *Infrared Photon Detectors*, SPIE Press, 1995.

[6] http://www.acreo.se/templates/Page____226.aspx

[7] M. Henini, M. Razeghi, *Handbook of Infrared Detection Technologies*, Elsevier Science Ltd., 2002.

[8] J. Piotrowski, F. Perry, "Designers Still Choose Mercury Cadmium Telluride", *Laser Focus World*, July 1997.

[9] R. S. Allgaier, "History of narrow-gap semiconductors and semimetals, 1945 -1965"*, Semicond. Sci. Technol.*, vol. 5, pp. S326-S333, 1990.

[10] A. Rogalski, "Infrared detectors: status and trends", *Progress in Quantum Electronics*, 27, pp. 59-210, 2003.

[11] P. Norton, "HgCdTe detectors", *Opto-Electronics Review*, 10(3), pp. 159-174, 2002.

[12] A. Rogalski, K. Adamiec, J. Rutkowski, *Narrow-Gap Semiconductor Photodiodes*, SPIE Press, 2000.

[13] P. Capper, *Narrow-gap II-VI Compounds for Optoelectronic and Electromagnetic Applications*, Chapman&Hall, 1997.

[14] P. Capper, *Properties of Narrow Gap Cadmium-based Compounds*, INSPEC, 1994.

[15] R. Rawe, A. Timlin, M. Davis, J. Devitt, M Greiner, "Advanced large format InSb IR FPA maturation at CMC Electronics," *Proceedings of SPIE*, vol. 5406, pp. 152-162, 2004.

[16] P. Castelein, F. Marion, J.-L. Martin, J. Baylet, N. Moussy, O. Gravrand, A. Durand, J.-P. Chamonal, and G. Destefanis, "A Megapixel HgCdTe MWIR Focal plane array with a 15 μm pitch," *Proceedings of SPIE*, vol. 5251, pp. 65-72, 2004.

[17] J. D. Kim, S. Kim, D. Wu, J. Wojkowski, J. Xu, J. Piotrowski, E. Bigan, and M. Razeghi, "8–13 μm InAsSb heterojunction photodiode operating at near room temperature," *Appl. Phys. Lett.*, vol. 67, pp. 2645-2647, 1995.

[18] J. J. Lee, J. D. Kim, and M. Razeghi, "Growth and characterization of InSbBi for long wavelength infrared Photodetectors," *Appl. Phys. Lett.*, vol. 70, pp. 3266-3268, 1997.

[19] Y. H. Choi, P. T. Staveteig, E. Bigan, and M. Razeghi, "Characterization of InTISb/lnSb grown by low-pressure metal-organic chemical vapor deposition on a GaAs substrate," *J. Appl. Phys.,* vol. 75, pp. 3196-3198, 1994.

[20] W. Cabanski, R. Breiter, R. Koch, W. Gross, K.-H. Mauk, W. Rode, J. Ziegler, H. Schneider, M. Walther, R. Oelmaier, "Third gen focal plane array IR detection modules at AIM," *Infrared Physics & Technology*, vol. 43, pp. 257-263, 2002.

[21] E. Brochier, P. Tribolet, P. Chorier, P. Costa, P. Fillon, "Cooled large IR staring arrays : towards third generation," *Proceedings of SPIE*, vol. 5251, pp. 26-36, 2004.

[22] C. M. Bacon, C. W. McMurtry, J. L. Pipher, W. J. Forrest, J. D. Garnett, D. Lee, and D. D. Edwallm "Characterization of Rockwell Scientific LWIR HgCdTe Detector Arrays," *Proceedings of SPIE*, vol. 5167, pp. 313-319, 2004.

[23] J. Piotrowski, A. Rogalski, "New generation of infrared photodetectors", *Sensors and Actuators A*, vol. 67, pp. 146-152, 1998.

[24] A. Rogalski, "Comparison of performance of quantum well and conventional bulk infrared photodetectors", *Infrared Physics and Technology*, vol. 38, pp. 295-310, 1997.

[25] A. Rogalski, "Heterostructure infrared photovoltaic detectors", *Infrared Physics and Technology*, vol. 41, pp. 213-238, 2000.

[26] P. R. Bratt, "HgCdTe heterojunctions", *J.Vac.Sci.Technol. A*, vol. 1(3), pp. 1687- 1691, July/Sept 1983.

[27] P. R. Bratt, T. N. Casselman, "Potential barriers in HgCdTe heterojunctions", *J.Vac.Sci.Technol. A*, vol. 3(1), pp. 238-245, Jan/Feb 1985.

[28] E. A. Kraut, "The effect of a valence-band offset on potential and current distributions in HgCdTe heterosturctures", *J.Vac.Sci.Technol. A*, vol. 7(2), pp. 420-423, Mar/Apr 1989.

[29] N. K. Dhar, M. Zandian, J. G. Pasko, J. M: Arias, J. H. Dinan, "Planar p-on-n HgCdTe heterostructure infrared photodiodes on Si substrates by molecular beam epitaxy", *Appl. Phys. Lett.*, vol. 70(13), pp. 1730-1732, 31 March 1997.

[30] G. Bahir, V. Garber, D. Rosenfeld, "Planar p-on-n HgCdTe heterostructure infrared photodiodes", *Appl. Phys. Lett.*, vol. 78(10), pp. 1331-1333, 5 March 2001.

[31] J. M. Arias, J. G. Pasko, M. Zandian, S. H. Shin, G. M. Williams, L. O. Bubulac, R. E. DeWames, W. E. Tennant, "Planar p-on-n HgCdTe heterostructure photovoltaic detectors", *Appl. Phys. Lett.*, vol. 62(9), pp.976-978, 1 March 1993.

[32] L. O. Bubulac, S. J. C. Irvine, E. R. Gertner, J. Bajaj, W. P. Lin, R. Zucca, "As diffusion in HgCdTe junction formation", *Semicond. Sci. Technol.*, vol. 8, pp. S270-S275, 1993.

[33] A. M. Turner, "HgTe contacts to p-HgCdTe", *J. Vac. Sci. Technol. B*, vol. 10(4), pp. 1534-1537, Jul/Aug 1992.

[34] A. Rogalski, R. Ciupa, "Theoretical modeling of long wavelength n^+-on-p HgCdTe photodiodes", *J. Appl. Phys.*, vol. 80(4), pp. 2483-2489, 15 August 1996.

[35] A. Rogalski, R. Ciupa, "Long-wavelength HgCdTe photodiodes: n^+-on-p versus p-on-n structures", *J. Appl. Phys.*, vol. 77(7), pp.3505-3512, 1 April 1995.

[36] www.indigosystems.com

[37] J. Baars, R. C. Keller, H. J. Richter, M. Seelmann-Eggebert, "The effect of CH_4/H_2 ECR plasma etching on the electrical properties of p-type $Hg_{1-x}Cd_xTe$", *Infrared Detectors for Remote Sensing: Physics, Material, and Detectors*, SPIE Proceedings vol. 2816, pp. 99–105, 1996.

[38] E. P. G. Smith, C. A. Musca, D. A. Redfern, J. M. Dell, and L. Faraone, "Reactive ion etching for mesa structuring in HgCdTe", *J. Vac. Sci. Technol. A*, vol. 17(5), 2503–2509, Sep/Oct 1999.

[39] E. P. G. Smith, C. A. Musca, D. A. Redfern, J. M. Dell, L. Faraone, "Reactive ion etching for mesa structuring in HgCdTe", *J. Vac. Sci. Tech. A*, vol. 17(5) *,* 2503–2509, Sep/Oct 1999.

[40] J. Wenus, J. Rutkowski, A. Rogalski, "Analysis of VLWIR HgCdTe photodiode performance", *Opto-Electronics Review*, vol. 11(2), pp. 143–149, 2003.

[41] W. E. Spicer, D. J. Friedman, G. P. Carey, "The electrical properties of metallic contacts on $Hg_{1-x}Cd_xTe$", *J. Vac. Sci. Technol. A*, vol. 6(4), pp. 2746–2751, Jul/Aug 1988.

[42] W. A. Beck, G. D. Davis, A. C. Goldberg, "Resistance and 1/f noise of Au, Al, and Ge contacts to (Hg,Cd)Te", *J. Appl. Phys.*, vol. 67(10), pp. 6340-6346, 15 May 1990.

[43] P. W. Leech, G. K. Reeves, "Specific contact resistance of indium ohmic contacts to n-type $Hg_{1-x}Cd_xTe$", *J. Vac. Sci. Technol. A*, vol. 10(1), pp. 105–109, Jan/Feb 1992.

[44] V. Krishnamurty, A. Simmons, C. R. Helms, "Studies of Au "ohmic" contacts to p-type $Hg_{1-x}Cd_xTe$", *J. Vac. Sci. Technol. A*, vol. 8(2), pp. 1147–1151, Mar/Apr 1990.

[45] V. Krishnamurty, A. Simmons, C. R. Helms, "Oxide interfacial layers in Au ohmic contacts to p-type $Hg_{1-x}Cd_xTe$", *Appl. Phys. Lett.*, vol. 56(10), pp. 925-927, 5 March 1990.

[46] T. Nguyen, C. A. Musca, J. M. Dell, J. Antoszewski, L. Faraone, "Modelling of dark currents in LWIR HgCdTe photodiodes", IEEE, pp. 157–160, 2002.

[47] J. Antoszewski, C. A. Musca, J. M. Dell, L. Faraone, M. Wagener, I. Switala, R. Oermann, "Small HgCdTe Infrared Detector Arrays from UWA", IEEE, pp.65 – 68, 2002.

[48] J. D. Friedman, "Metal interfaces with mercury cadmium telluride", *Ph.D. Thesis*, Stanford University, Department of Applied Physics, August 1987.

[49] S. Özer, "InSb and InAsSb infrared photodiodes on alternative substrates and InP/InGaAs quantum well infrared photodetectors: pixel and focal plane array performance", *Ph.D. Thesis*, Middle East Technical University, Department of Electrical and Electronics Engineering, May 2005.

[50] Y. Nemirovsky, R. Fastov, M. Meyassed, A. Unikovsky, "Trapping effects in HgCdTe", *J. Vac. Sci. Technol. B*, vol. 9(3), pp. 1829–1839, May/Jun 1991.

[51] V. Gopal, S. K. Singh, R. M. Mehra, “Analysis of dark current contributions in mercury cadmium telluride junction diodes”, *Infrared Physics & Technology*, vol. 43, pp. 317–326, 2002.

[52] Y. Nemirovsky, D. Rosenfeld, R. Adar, A. Kornfeld, “Tunneling and dark currents in HgCdTe photodiodes”, *J. Vac. Sci. Technol. A*, vol. 7(2), pp. 528–535, Mar/Apr 1989.

[53] J. D. Vincent, *Fundamentals of Infrared Detector Operation and Testing*, Wiley Press, 1990.

[54] Y. Nemirovsky, U. Univkovsky, “Tunneling and 1/f noise currents in HgCdTe photodiodes”, *J. Vac. Sci. Technol. B*, vol. 10(4), pp. 1602–1610, Jul/Aug 1992.